SARS-CoV-2 restructures host chromatin architecture

Check for updates

Ruoyu Wang [1,2,6], Joo-Hyung Lee[1,6], Jieun Kim[3,4], Feng Xiong[1], Lana Al Hasani[1,2], Yuqiang Shi[1], Erin N. Simpson[1,2], Xiaoyu Zhu[1], Yi-Ting Chen[1,2], Pooja Shivshankar[1,3,4], Joanna Krakowiak[1], Yanyu Wang[3,4], David M. Gilbert [5], Xiaoyi Yuan[3,4], Holger K. Eltzschig [2,3,4] & Wenbo Li[1,2]

Some viruses restructure host chromatin, influencing gene expression, with implications for disease outcome. Whether this occurs for SARS-CoV-2, the virus causing COVID-19, is largely unknown. Here we characterized the 3D genome and epigenome of human cells after SARS-CoV-2 infection, finding widespread host chromatin restructuring that features widespread compartment A weakening, A–B mixing, reduced intra-TAD contacts and decreased H3K27ac euchromatin modification levels. Such changes were not found following common-cold-virus HCoV-OC43 infection. Intriguingly, the cohesin complex was notably depleted from intra-TAD regions, indicating that SARS-CoV-2 disrupts cohesin loop extrusion. These altered 3D genome/epigenome structures correlated with transcriptional suppression of interferon response genes by the virus, while increased H3K4me3 was found in the promoters of pro-inflammatory genes highly induced during severe COVID-19. These findings show that SARS-CoV-2 acutely rewires host chromatin, facilitating future studies of the long-term epigenomic impacts of its infection.

The three-dimensional (3D) folding of mammalian chromatin influences transcription, DNA replication, recombination and DNA damage repair[1–3], with obvious effects on how cells behave and function. Regulation of host chromatin architecture has been used by viruses to antagonize host defence or to exert long-term influences, such as viral latency[4–6]. Severe acute respiratory syndrome coronavirus 2 (SARS-CoV-2) causes COVID-19 and has made >700 million infections worldwide. Several viral proteins encoded by SARS-CoV-2 have been shown to associate with chromatin or chromatin factors[7,8]. However, whether and how SARS-CoV-2 infection affects host chromatin architecture is underexplored.

Chromatin architecture is structured through several layers such as A/B compartments, topological associating domains (TADs), and chromatin loops[2,9] (Extended Data Fig. 1a,b). A/B compartments largely overlap with transcriptionally active/inactive chromatin, respectively[9,10]. They are suggested to be formed, at least in part, via homotypic attractions between chromatin regions of similar epigenetic features[9–11], which may function in transcription control through concentrating or sequestering specific regulatory factors[11]. For TADs and loops, CTCF (CCCTC-binding factor, a highly conserved zinc-finger protein) and the cohesin complex are the two main regulators[3]. Growing evidence indicates that cohesin acts via a 'loop extrusion' process[3]. These two mechanisms can crosstalk—the formation of TADs by loop extrusion appears to antagonize compartmentalization[3,9,12,13]. How chromatin architectures are rewired

[1]Department of Biochemistry and Molecular Biology, McGovern Medical School, The University of Texas Health Science Center at Houston, Houston, TX, USA. [2]The University of Texas MD Anderson Cancer Center UTHealth Houston Graduate School of Biomedical Sciences, The University of Texas Health Science Center at Houston, Houston, TX, USA. [3]Department of Anesthesiology, Critical Care and Pain Medicine, McGovern Medical School, The University of Texas Health Science Center at Houston, Houston, TX, USA. [4]Center for Perioperative Medicine, McGovern Medical School, The University of Texas Health Science Center at Houston, Houston, TX, USA. [5]Laboratory of Chromosome Replication and Epigenome Regulation, San Diego Biomedical Research Institute, San Diego, CA, USA. [6]These authors contributed equally: Ruoyu Wang, Joo-Hyung Lee. ✉e-mail: Wenbo.li@uth.tmc.edu

in pathological conditions including infectious diseases remains incompletely understood. Here we sought to understand the impacts of the pandemic-causing SARS-CoV-2 on host chromatin by comprehensively mapping the chromatin architectures of human cells after infection using high-throughput chromosome conformation capture (Hi-C) 3.0 and chromatin immunoprecipitation (ChIP-seq) methods. We uncovered extensive chromatin restructuring upon SARS-CoV-2 infection, with implications for understanding COVID-19 disease gene alteration and epigenetic perturbation in the host.

Results

SARS-CoV-2 infection restructures the host cell genome

To study chromatin organization during SARS-CoV-2 infection, we first determined the optimal infection conditions. Our approaches use cell populations and thus require a high ratio of infection of the host cells. In human A549 cells expressing ACE2 (A549-ACE2) (Fig. 1a) that were infected with SARS-CoV-2 (multiplicity of infection (MOI): 0.1), approximately 90% of RNA-sequencing (RNA-seq) reads aligned to the viral genome at 24 h post-infection (24 hpi), indicating a high level of infection (Extended Data Fig. 1c). Immunofluorescence of the viral spike protein verified a high infection ratio (Extended Data Fig. 1d,e). We did not observe cell apoptosis (Extended Data Fig. 2a–c). We therefore focused on cells at 24 hpi to study host chromatin changes.

We then used Hi-C 3.0 (ref. [14]), a recently improved version of in situ Hi-C, to analyse SARS-CoV-2-infected A549-ACE2 cells at 24 hpi or mock-infected cells (Mock). We sequenced the libraries to ~2.6 billion read-pairs (Supplementary Table 1), generating ~630–770 million unique contact pairs for each condition. There was high concordance between replicates (Extended Data Fig. 2d–f). We combined the replicates for the subsequent analysis, and still refer to them as Hi-C.

Hi-C revealed a widespread alteration of the 3D genome by SARS-COV-2. The near-diagonal short-range contacts were weakened globally, as exemplified in Fig. 1b (black arrowheads). In contrast, long-range chromatin contacts far away from the diagonal were often deregulated (increased or decreased for different regions, grey box) (Fig. 1b). A Pearson correlation map of Hi-C interactions consistently revealed these changes (Fig. 1c), which also suggests altered chromatin compartmentalization. A zoomed-in view of an example region of ~0.7 Mb showed that rectangle-shaped chromatin domains (cyan arrowheads) are often weakened, whereas chromatin loops ('dot' off the diagonal, pink arrowheads) are deregulated (Fig. 1d). A P(s) curve demonstrates that SARS-CoV-2 elicited a global reduction in short-distance chromatin contact (<560 kb), a moderate increase in mid-to-long-distance interactions (~560 kb–8.9 Mb) and enhanced interactions for far-separated regions (>28 Mb) (Fig. 1e). Intriguingly, inter-chromosomal contacts were generally increased by viral infection, as shown by the fold changes in pairwise interactions between any two chromosomes, or by trans-vs-cis contact ratios (Extended Data Fig. 2g,h). The enhancement of both inter-chromosomal interactions and extremely long-distance (>28 Mb) intra-chromosomal interactions (Fig. 1e) suggests changes in chromatin compartmentalization[12,15].

We investigated whether the observed changes are uniquely induced by SARS-CoV-2 infection, or are general phenomena upon coronavirus infection or innate immune signalling. We conducted Hi-C 3.0 after three additional treatments: (1) heat-inactivated SARS-CoV-2 virus (HI-WA1); (2) infection by a human common-cold coronavirus HCoV-OC43 (ref. [16]), which can efficiently infect A549 (refs. [17,18]); and (3) a synthetic double-stranded RNA viral mimic, polyinosinic:polycytidylic acid or poly (I:C). We used a 0.5 MOI of HCoV-OC43 to achieve >90% infection rate at 24 hpi; and for poly (I:C), quantitative PCR with reverse transcription (RT–qPCR) validated the induction of target genes after treatment (Extended Data Fig. 3a–c). An initial P(s) curve analysis revealed that none of these additional treatments elicited changes similar to those observed upon SARS-CoV-2 infection (Fig. 2a,b). Particularly, HI-WA1 elicited almost no change in 3D genome architecture, whereas HCoV-OC43 and Poly (I:C) infection had mild effects (Fig. 2a,b).

SARS-CoV-2 infection alters chromatin compartmentalization

Principal component analysis (PCA) of Hi-C data can divide genomes into A/B compartments[9,19], which largely overlap euchromatin/heterochromatin[11]. Analysing a 100-kb-binned Hi-C matrix, we found notable defects of chromatin compartmentalization in SARS-CoV-2-infected cells (Fig. 2c). Overall, PCA E1 scores exhibited a general reduction in infected cells (that is, moving below the diagonal, Fig. 2c), suggesting a pervasive weakening of the A compartment and/or A-to-B switching. By measuring E1 changes[20], we found that ~30% of genomic regions exhibited compartmental weakening or switching after SARS-CoV-2 infection (Extended Data Fig. 4a). The changes commonly displayed features of weakened A (for example, A to weaker A or A to B) or strengthening of the B compartment (B to stronger B). Among these, A to weaker A is the most common (~18% of the genome, Extended Data Fig. 4a). Examples are shown in Fig. 2d. These changes indicate that SARS-CoV-2 infection pervasively weaken the euchromatin of the host cells.

We evaluated the epigenetic features of the altered regions to understand the susceptibility to compartmental changes due to infection. By ranking E1-score changes for each genomic bin, we sorted them into six categories (Fig. 2e). Those showing E1-score increase were dubbed as 'A-ing' bins and those showing decrease as 'B-ing' bins. We generated ChIP-seq data of representative histone marks (H3K27ac, H3K4me3, H3K9me3 and H3K27me3) and polymerase II (Pol2) in A549-ACE2 cells, and examined the epigenetic features of these six categories of bins. This analysis revealed that the 'B-ing' genomic regions are those originally enriched in active chromatin marks (such as H3K27ac), whereas the 'A-ing' genomic regions are those originally enriched in repressive histone marks (particularly H3K27me3) (Fig. 2f). These results suggest that the originally well-segregated A or B compartments were losing their identity, indicating defective chromatin compartmentalization. Indeed, as shown in Fig. 1c, defective compartmentalization manifests as increases in inter-compartmental interactions formed between regions of A and B and decreases in those formed within A or B (black and cyan arrowheads in Fig. 1c, respectively). A saddle plot that depicts genome-wide inter-compartment interactions shows that such changes are global (Fig. 3a)[10,13]. There is a strong reduction in A–A homotypic interactions accompanied by a gain in A–B mixing, while B–B interactions were not changed (Fig. 3a). Weakened compartmentalization can also be seen between

---

Fig. 1 | SARS-CoV-2 restructures the host 3D genome. a, The experimental design of this work. Created with BioRender.com. **b**, Hi-C 3.0 contact matrices of an example region (chr9: 100–130 Mb, hg19) in mock or infected conditions. Black arrowheads denote reduced short-distance interactions along the diagonal. Grey boxes show regions with altered compartmentalization. Bin size, 80 kb. **c**, Pearson correlation matrices of Hi-C 3.0 in the same region as in **b**. Arrowheads point to regions with virus-altered A–B (black) or A–A (cyan) compartmental interactions. Bin size, 80 kb. Colour scales indicate Pearson correlation coefficient (left and middle), and changes in the correlation matrices after infection (SARS-CoV-2/Mock, Pearson) are shown on the right. **d**, Zoom-in

Hi-C snapshots of a 700 kb region in **b** and **c** (chr9: 95.7–96.4 Mb, hg19). Pink and cyan arrowheads show changed dot-shaped loops and domains, respectively. Bin size, 5 kb. **e**, Top: P(s) curve showing the relationship between the Hi-C contract frequency (P) of intra-chromosomal interactions ranked by genomic distance (s) in both mock (grey) and SARS-CoV-2 (red) conditions. Bottom: log₂FC of Hi-C contact frequency ranked by distances (infection/mock), with dotted lines marking the crossing points of the two curves. In **b** and **d**, colour scales indicate Hi-C contact frequencies (left and middle), and log₂FC of SARS-CoV-2/mock contact frequencies (right).

chromosomes; for example, chromosomes 17 and 18, where originally well-separated A–A/B–B homotypic interactions were compromised but A–B interactions enhanced (Extended Data Fig. 4b).

In comparison with SARS-CoV-2, the other treatments caused little or mild changes to compartments. Saddle plot analyses showed that HI-WA1 and poly (I:C) elicited negligible changes, whereas
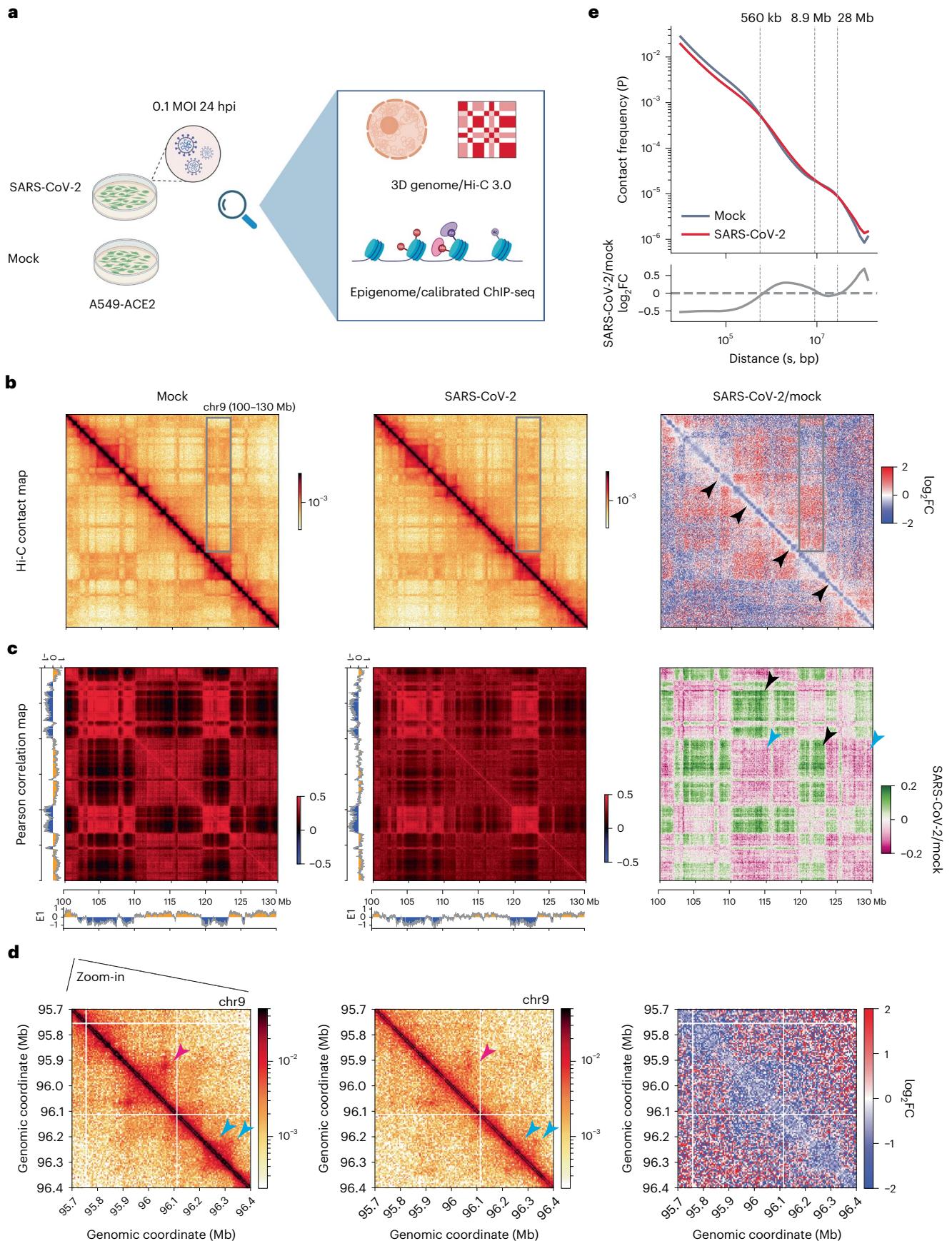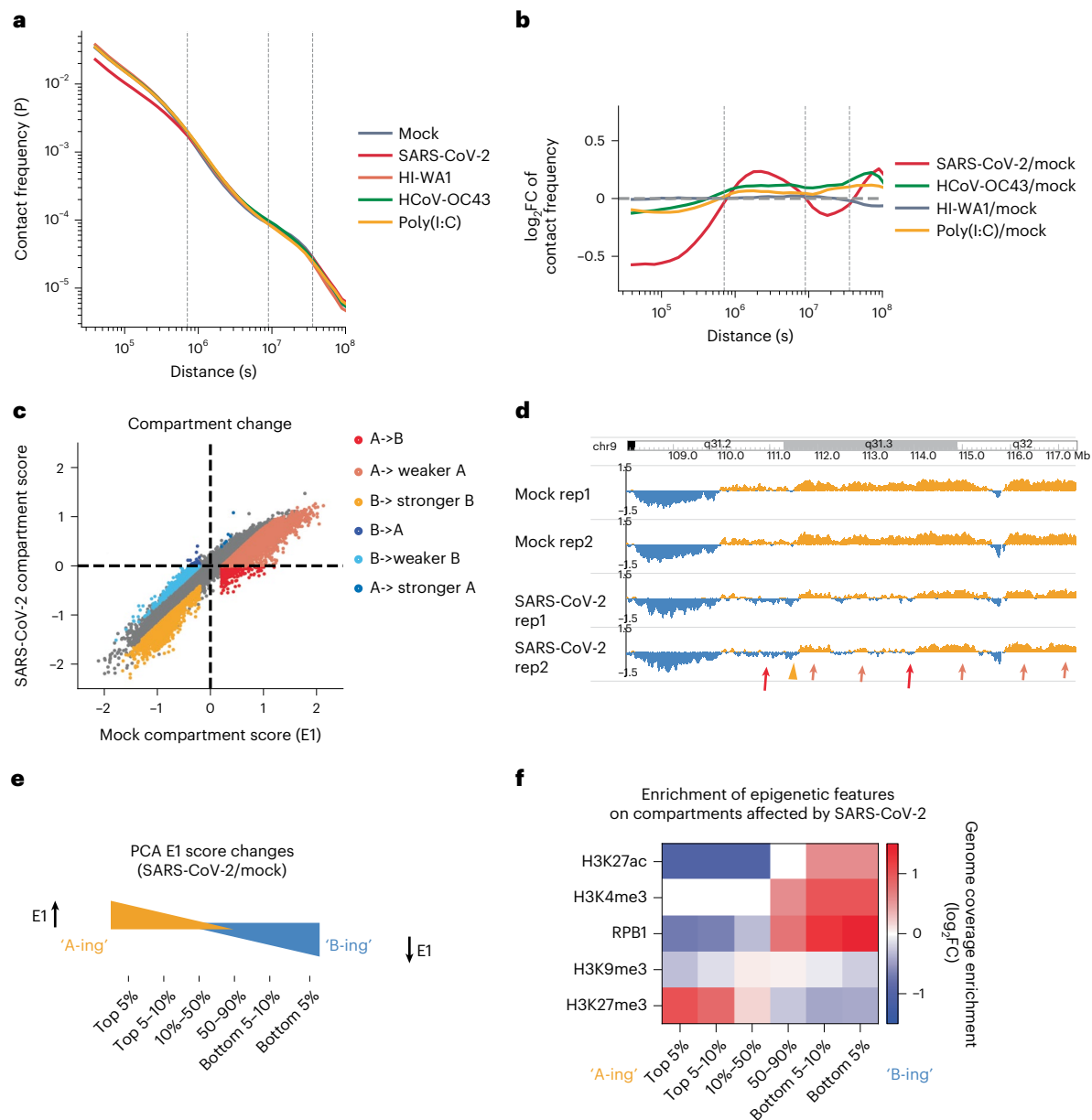
Fig. 2 | Compartment A weakening by SARS-CoV-2. a, P(s) curve showing the relationship between contact frequency (P) and distance (s) of mock, SARS-CoV-2, HI-WA1 (heat-inactivated SARS-CoV-2), HCoV-OC43 and poly (I:C) Hi-C datasets. **b**, $\log_2$ fold changes (FC) of P(s) curves showing the differences in Hi-C contacts between SARS-CoV-2/Mock, HI-WA1/Mock, HCoV-OC43/Mock or poly(I:C)/Mock. **c**, A scatterplot showing the compartmental E1 scores of genome-wide 100 kb bins in mock or SARS-CoV-2-infected cells. Six categories of bins based on E1 changes were coloured-coded. **d**, A snapshot of PCA E1 tracks at an example region (chr9: 108–118 Mb). Rep1/Rep2 are replicates. Orange or blue indicates A (E1 score >0) or B compartment (E1 score <0), respectively. Arrows and arrowheads exemplify regions with compartmental changes (with colours matching **a**). **e**, A diagram showing the categories of bins with changes in A/B compartmental scores, which are referred to as 'A-ing' (E1 scores increase) or 'B-ing' (E1 scores decrease) after virus infection. **f**, Heatmaps showing enrichment of histone marks or RNA Pol2 (RPB1) on the six categories of genomic bins defined in **e**, which signifies their epigenomic features over the genome background. Scale indicates $\log_2$-transformed fold enrichment.

HCoV-OC43 caused mild weakening of A–A interaction (Extended Data Fig. 4c–e). We further calculated compartmental shifting in these samples at 100 kb bin resolution. HI-WA1 and poly(I:C) again caused negligible changes, whereas HCoV-OC43 infection resulted in ~13% of genome bins showing compartmental alteration (Extended Data Fig. 5a–c). We compared the changes due to HCoV-OC43 versus those due to SARS-CoV-2, finding limited overlaps (Extended Data Fig. 5d–j). These results together support that SARS-CoV-2 infection caused unique and dramatic chromatin restructuring at A/B compartmental levels. Hereafter, we focus on SARS-CoV-2 infection and only occasionally compare the differences between SARS-CoV-2 effects and those of the other virus or stimulus.

SARS-CoV-2 changes the host epigenome and reduces H3K27ac

Chromatin in the A compartment enriches for active histone modifications, while chromatin in the B compartment enriches for repressive histone marks[11,19]. To mechanistically understand the observed changes, we examined active and repressive histone modifications (active: H3K4me3 and H3K27ac; repressive: H3K9me3
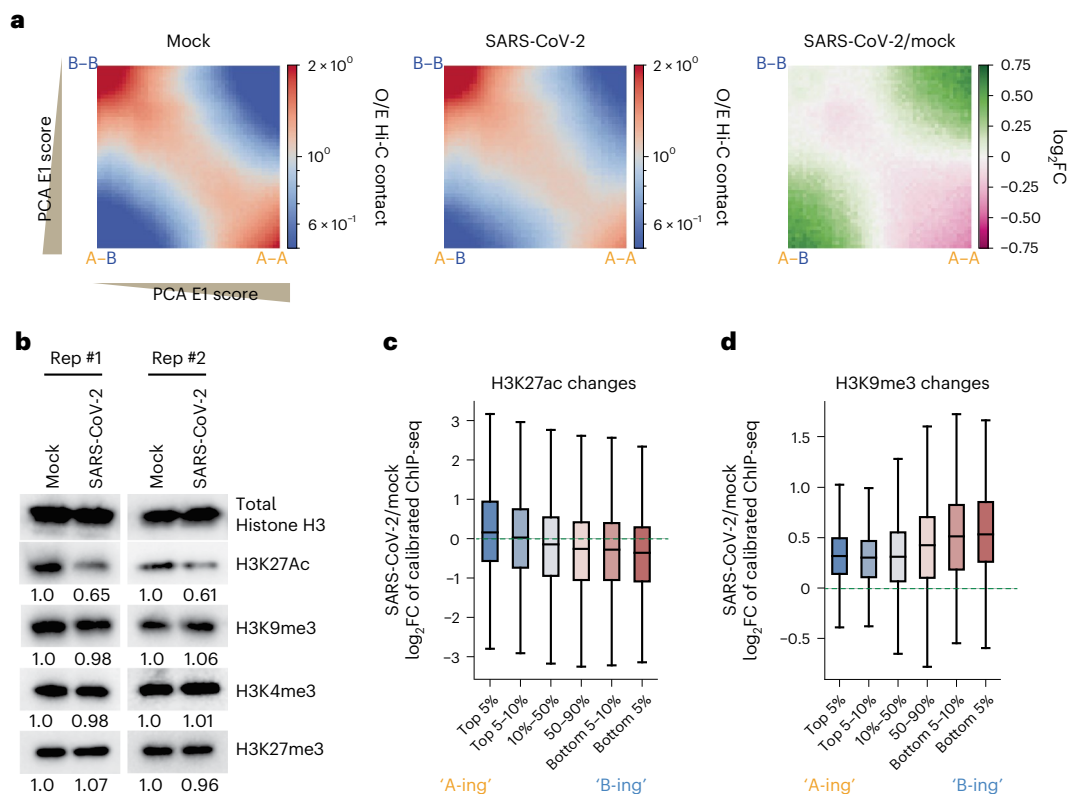
Fig. 3 | Compartment A–B mixing and epigenome reprogramming. a, Saddle plots showing chromatin compartmentalization between genomic regions ranked by their E1 scores (genome was divided into 50 total bins). A–A homotypic interactions are shown in the lower right; A–B interactions are in the upper right and lower left. Differential compartmental interactions are shown on the right as log$_2$FC, SARS-CoV-2/Mock. **b**, Western blots showing the abundances of total histone H3 or several modifications in Mock and SARS-CoV-2-infected (24 hpi) cells. Total histone H3 served as a sample processing control and was run on a separate membrane with the same amount of protein loaded. Quantification was done by ImageJ and is shown at the bottom. Rep #1 and #2 are two replicates. **c,d**, Boxplots showing the log$_2$FC of calibrated ChIP-seq signals of H3K27ac (**c**) (from left to right, n = 896, 1,116, 16,877, 25,535, 3,739 and 3,990 peaks) and H3K9me3 (**d**) (from left to right, n = 1,333, 1,332, 10,660, 10,660, 1,332 and 1,333 bins) for the six categories of genomic bins with varying compartmental changes (as in Fig. 2e). For boxplots, the centre lines represent medians; box limits indicate the 25th and 75th percentiles; and whiskers extend 1.5 times the IQR from the 25th and 75th percentiles.

and H3K27me3) before and after infection (Fig. 1a). Western blots showed that most of these modifications remain unaltered, but surprisingly, active histone mark H3K27ac displayed a consistent and notable reduction (Fig. 3b). We conducted spike-in calibrated ChIP-seq[21] to precisely quantify epigenomic changes (Extended Data Fig. 6a). By calculating the ratios of ChIP-seq reads aligned to the human versus to the mouse genome (that is, spike-in), we consistently observed a reduction in H3K27ac on the host chromatin by ~40–45% (Extended Data Fig. 6b,f), which agrees with western blots (Fig. 3b). A second active mark, H3K4me3, did not exhibit overall changes, but there were moderate gains in repressive histone marks, such as H3K9me3, after infection (Extended Data Fig. 6c–i).

The epigenome reprogramming after SARS-CoV-2 infection resonates with the pervasive decrease in A–A compartmental interactions and weakening of the A compartment (Figs. 2c and 3a). We overlaid histone mark alterations on the six categories of genomic regions that bear compartmental changes (Fig. 2e), finding that the most 'B-ing' regions exhibit stronger reduction in H3K27ac (Fig. 3c), whereas the most 'A-ing' regions exhibit stronger increase in H3K9me3 (Fig. 3d). An example is shown in Extended Data Fig. 6j, where H3K27ac reduces and H3K9me3 increases, correlating with compartmental changes: weakened A–A contacts and increased A–B mixing, respectively. Because attractions between homotypic chromatin regions were suggested to be important for compartmentalization[9,11–13], our results support the notion that SARS-CoV-2 disrupts host chromatin compartmentalization, at least in part, via reprogramming of chromatin modifications.

Weakening of intra-TAD interactions upon SARS-CoV-2 infection

We then examined chromatin architectures at finer scales (10 kb–1 Mb), namely TADs and chromatin loops[2,3,9]. A pronounced phenomenon (for example, Figs. 1d and 4a) is that *cis* interactions within TADs (intra-TAD) were reduced by infection, whereas the contacts beyond TADs (out of the rectangles) were unchanged or increased. Examining this genome-wide, we calculated the insulation scores (IS)[22] and identified 4,094 TADs. Aggregation domain analyses (ADA) verified the substantial weakening of intra-TAD *cis* interactions, which accompanies unchanged or increased *cis* interactions outside of TADs (Fig. 4b). Quantification of all intra-TAD contacts showed dramatic reduction (Fig. 4c). Interestingly, weakened intra-TAD contacts were not accompanied by severe loss of TAD identities, that is, the boundaries of TADs were largely unchanged (Fig. 4a,b middle panels). Indeed, insulation scores of all TAD boundaries were only mildly affected by SARS-CoV-2 (Fig. 4d). TAD changes due to the other virus/stimulus are negligible; for HCoV-OC43, a trend of intra-TAD reduction was observed but the magnitude is mild (Fig. 4c and Extended Data Fig. 5k–m). These results indicate that strong inhibition of intra-TAD chromatin contacts is a particular feature of SARS-CoV-2.

Cohesin depletion from intra-TAD regions

To further understand the reduction in intra-TAD interactions during SARS-CoV-2 infection, we examined the protein levels or chromatin binding of CTCF and cohesin, the two main regulators of

TADs[2,3,9]. Western blots for CTCF and RAD21 showed no reduction in protein abundances (Extended Data Fig. 7a). Peak calling from calibrated ChIP-seq for each factor resulted in ~40,000–60,000 peaks (Extended Data Fig. 7b–e). Importantly, for two cohesin subunits, 40.4% (27,152/67,140) of RAD21 sites and 31.8% (20,837/65,379) of SMC3 sites were reduced after SARS-CoV-2 infection (Extended Data Fig. 7c,d). In contrast, only small percentages of their binding sites were gained, that is, 2.2% (1,510/67,140) for RAD21 sites and 3.1% (2,034/65,379) for SMC3 (Extended Data Fig. 7c,d). Moderate changes in CTCF binding were observed, with 10.6% (4,853/45,530) of sites lost and 10.0% (4,555/45,530) of sites gained (Extended Data Fig. 7e). These changes can be seen in an example TAD (Fig. 4e, same as the region in Fig. 4a).

We divided all TADs into six categories on the basis of their sensitivity to SARS-CoV-2 infection (that is, quantitative reduction of intra-TAD contacts, Extended Data Fig. 7g), and examined the chromatin features of these categories. Notably, the more sensitive the TADs are to SARS-CoV-2 infection (that is, more dramatic weakening of intra-TAD contacts), the higher enrichment of cohesin and NIPBL they bear in Mock condition (Fig. 4f), suggesting that TADs with high loads of cohesin/NIPBL make them more susceptible to cohesin depletion and intra-TAD weakening. Indeed, the top 10% most virus-weakened TADs are associated with a more dramatic loss of cohesin from the intra-TADs regions (Fig. 4g). In addition, compared with the TAD boundaries, cohesin loss was more dramatic at the intra-TAD regions (Fig. 4e,g). CTCF was minimally impacted at both TAD boundaries and intra-TAD regions (Fig. 4e,g). These data together indicate that SARS-CoV-2 preferentially disrupts cohesin inside TADs, but largely leaves the TAD structures intact, which is consistent with the Hi-C analysis shown in Fig. 4b,d. Because NIPBL, a key factor that loads cohesin to chromatin[3], was found to be enriched in the most virus-weakened TADs (Fig. 4f), we examined its binding by ChIP-seq, finding dramatic inhibition by infection (Extended Data Fig. 7f). NIPBL reduction correlated with the extent of intra-TAD weakening (Fig. 4h). These results support the idea that inhibited NIPBL binding to chromatin upon SARS-CoV-2 infection underlies cohesin depletion from intra-TAD regions.

Besides cohesin, H3K27ac was also more enriched in SARS-CoV-2-sensitive TADs, but heterochromatin marks did not show obvious correlation (Fig. 4f). We examined the changes in epigenetic marks in the six different categories of TADs, finding that while the H3K27ac level was globally reduced (Fig. 3b), the reduction was consistent among all TADs (Extended Data Fig. 7h). In contrast, H3K9me3, but not another heterochromatin mark H3K27me3, was gained substantially more in the most weakened TADs (Extended Data Fig. 7i,j). This correlation suggests that increased H3K9me3 may play a role in cohesin depletion and intra-TAD weakening caused by SARS-CoV-2.

SARS-CoV-2 infection affects dot-shaped chromatin loops

A dot-shaped loop is a prominent feature in Hi-C that often forms between convergent CTCF sites[9,19]. The definition and functions of chromatin loops are debatable[9]. Some work has defined dot-shaped loops in Hi-C as structural loops[23]. In this study, we refer to dot-shaped structures as loops and define enhancer–promoter contacts using Hi-C interaction strength (see Methods). By call-dots[24], we identified 11,926 loops at 5–10 kb resolution, with examples shown in Fig. 5b. Globally, aggregation peak analyses (APA) showed that chromatin loops were not overtly affected by infection (Extended Data Fig. 8a). Quantitatively (false discovery rate (FDR) < 0.1), we found that 2.96% (353/11,926) of loops were weakened, whereas 4.70% (560/11,926) gained strength (Extended Data Fig. 8b,c). The weakened loops are mostly short-range loops (median size 150 kb), while interestingly, the gained ones are much longer (median size 417.5 kb, Extended Data Fig. 8d). This is reminiscent of the fact that long-distance chromatin interactions were enhanced by infection (Fig. 1e). Compared with loops strengthened after SARS-CoV-2 infection, the anchors of weakened loops showed more dramatic cohesin depletion after infection and are farther away from TAD boundaries (Extended Data Fig. 8e,f), suggesting that virus-weakened loops are probably a consequence of defective cohesin loop extrusion inside TADs.

Genome/epigenome restructuring and gene deregulation

COVID-19 patients with severe symptoms often show two immuno-pathological features: a delayed or weakened innate immune response (that is, interferon gene expression) and an exacerbated production of pro-inflammatory cytokines (for example, IL6)[25]. Our 3D genome/epigenome maps provided an opportunity to understand the deregulation of these genes. Our Pol2 ChIP-seq recapitulated these two features (Fig. 5a), indicating that their deregulation occurs transcriptionally. Their changes can also be seen by RNA-seq (Extended Data Fig. 9a). Compared with interferon-beta (IFN-β) stimulus, SARS-CoV-2 infection elicited limited activation of interferon response genes (hereafter IFN genes) but strong increases in pro-inflammatory genes (hereafter PIF genes) (Fig. 5a). Key examples include *IFIT1/2/3/5*, *DDX58* (also known as *RIG-I*) (for IFN), and *IL6* or *CXCL8* (for PIF) (Extended Data Fig. 9b,c). Inspection of IFN gene loci revealed remarkable changes in chromatin architecture by SARS-CoV-2: (1) the dot-shaped loops were often diminished, and the chromatin contacts (which include most enhancer–promoter contacts) throughout the hosting TAD reduced; (2) cohesin occupancy within the hosting TADs was decreased; (3) H3K27ac was notably reduced at many nearby putative enhancers (Fig. 5b and Extended Data Fig. 9d,e). Both enhancer–promoter contacts and enhancer activities may contribute to gene transcriptional outputs[26]; hence, we modified and applied the activity-by-contact (ABC) algorithm to model how 3D genome/epigenome changes underlie virus rewiring of host transcription (Fig. 5c). The ABC scores well modelled the weakened transcriptional outputs of IFN genes (Pearson's correlation coefficient $R = 0.61$, Fig. 5d). In contrast, poor prediction was achieved if only one of the two features was considered (Extended Data Fig. 9f,g). We functionally tested virus-weakened enhancers by
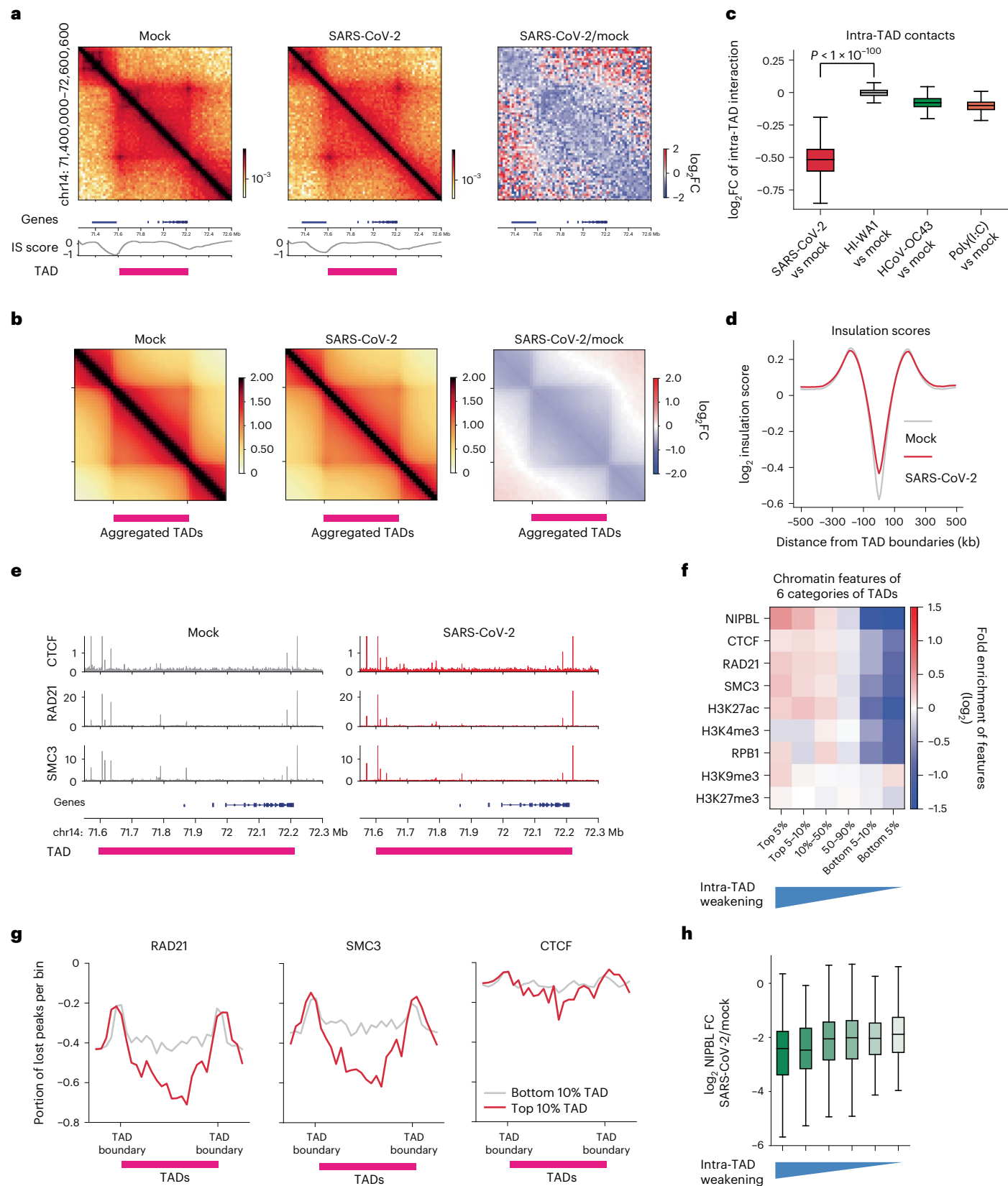
Fig. 4 | SARS-CoV-2 weakens chromatin contacts and cohesin loading in intra-TAD regions. a, Hi-C matrices (bin size, 5 kb) at the indicated region (hg19), its log₂FC after infection (right panel), RefSeq gene tracks (bottom), the insulation score (IS, bottom) and TAD location (pink bars). Genomic coordinate is indicated on the left vertical axis. **b**, ADA showing genome-wide reduction in intra-TAD interactions after infection. Right: log₂FC. TAD location is denoted by a pink bar. The plots include additional 0.5×TAD on each side for quantification. In **a** and **b**, colour scales indicate aggregated Hi-C contact frequencies (left and middle), and log₂FC of SARS-CoV-2/Mock aggregated contact frequencies (right). **c**, Boxplots showing log₂FCs of intra-TAD Hi-C interactions after several treatments in comparison to the Mock (from left to right, $n = 4,094, 4,094, 4,094$ and $4,094$). $P = 0$, calculated using a two-sided Mann–Whitney U test. **d**, A profile plot of insulation scores calculated from all TAD boundaries in two conditions. **e**, Snapshots of CTCF, RAD21 and SMC3 ChIP-seq tracks in two conditions at an example TAD region. **f**, A heatmap showing the enrichment of cohesin/CTCF or epigenetic marks in six categories of TADs ranked by reduction in intra-TAD interactions (see Extended Data Fig. 7g). The blue triangle at the bottom denotes the severity of intra-TAD weakening. **g**, Meta-profiles showing the portions of ChIP-seq peaks reduced by SARS-CoV-2, and the positioning of the changes in TADs. Line plots show the degree of weakened peaks relative to hosting TADs (0.25×TAD on each side out of TAD). Red lines indicate peak reduction for the top 10% weakened TADs; grey lines indicate peak reductions in the 10% least weakened TADs. The y axis indicates the portion of lost peaks (for example, −0.6 indicates that 60% ChIP-seq peaks in that bin were reduced). **h**, Boxplots showing the log₂FC of NIPBL ChIP-seq signals (SARS-CoV-2/Mock) in the six categories of TADs ranked by the severity of intra-TAD weakening (from left to right, $n = 133, 155, 1,262, 1,324, 163$ and 108 peaks). For boxplots in **c** and **h**, the centre lines represent medians; box limits indicate the 25th and 75th percentiles; and whiskers extend 1.5 times the IQR from the 25th and 75th percentiles.

CRISPRi in two loci, finding that IFN genes were indeed transcriptionally inhibited from responding to viral mimicry (Fig. 5e and Extended Data Fig. 9d,h). We validated a role of cohesin in this process by using an acute RAD21 degron system[27], finding that stimulus-induced IFN gene activation was dampened (Fig. 5f). This is consistent with the notion that cohesin depletion has a mild impact on basal gene transcription[12,13], but can substantially affect stimuli-induced transcription[28–30]. These results supported the finding that weakened 3D chromatin contacts and enhancer activity together shaped the transcriptional inhibition of IFN genes by SARS-CoV-2. Interestingly, HCoV-OC43

infection did not elicit weakening of enhancer features (H3K27ac) and chromatin contacts at IFN genes (Fig. 5g).

For PIF genes, while ABC scores showed good correlation, their true transcriptional levels after SARS-CoV-2 infection were often several-fold higher than ABC scores (Extended Data Fig. 10a,b). As shown for *IL6* and *CXCL8* encoding key pathological cytokines, they display similar changes as IFN genes: both enhancer activities (H3K27ac) and intra-TAD contacts were reduced (Fig. 6a and Extended Data Fig. 10c), albeit they were strongly upregulated (Extended Data Fig. 9a–c). We therefore re-examined our epigenome data for the PIF loci, finding a unique and dramatic gain in H3K4me3 at their promoters (Fig. 6a and Extended Data Fig. 10c), which did not occur on IFN genes (Fig. 5b and Extended Data Fig. 9d,e). H3K4me3 at promoters may play a causal role in transcription[31,32]. Globally, H3K4me3 exhibited relatively limited changes due to SARS-CoV-2 infection: 5.8% (1,843/31,761) of sites showed increases and 3.5% (1,104/31,761) showed decreases (Extended Data Fig. 10d). Interestingly, genes close to gained H3K4me3 sites enrich for key pathways in COVID-19 pathology[33] (for example, TNF-alpha or TGF-beta signalling, Extended Data Fig. 10e). We revised the ABC algorithm by including H3K4me3 changes at promoters (Fig. 5c), and a revised ABC-P² score better modelled PIF genes' transcriptional induction (Fig. 6b and Extended Data Fig. 10b).

We tested the role of PIF promoters by using an mCherry reporter, finding that the *IL6* promoter alone can elicit gene activation upon infection (Fig. 6c,d). Intriguingly, promoters with virus-augmented H3K4me3 display motif enrichment of specific transcriptional factors, such as IRF1/2 or Jun/AP1 (Extended Data Fig. 10f), suggesting their potential roles in PIF promoter activation. In notable contrast, HCoV-OC43-infected cells showed little or no changes in H3K4me3 at PIF promoters (Extended Data Fig. 10g). These results together suggest that pro-inflammatory genes are induced by SARS-CoV-2 through a unique process involving H3K4me3 to augment promoter activity.

Discussion

Here we found that SARS-CoV-2 infection notably restructures 3D host chromatin, featuring widespread compartment A weakening and A–B mixing, and global reduction in intra-TAD chromatin contacts (Fig. 6e). The epigenome is also altered, including a global reduction in active chromatin mark H3K27ac and a specific increase in H3K4me3 at pro-inflammatory gene promoters. Interestingly, these changes were quite unique to SARS-CoV-2 compared with infection by common-cold coronavirus or immune stimuli. What we characterized here represents a direct cell-autonomous effect elicited by SARS-CoV-2 on the host chromatin. Consistent with our results, some compartmental changes after infection have also been reported[34].

In parallel, SARS-CoV-2 also imposes non-cell-autonomous effects on the 3D genome[35]. An important unanswered question is exactly how SARS-COV-2 infection restructures host chromatin and whether viral regulators are involved. In this light, ORF8 was recently found to disrupt the host epigenome[7], suggesting that specific viral factors could confer the chromatin restructuring we discovered in this work.

Mechanistically, SARS-CoV-2 infection depleted the cohesin complex, in a pervasive but selective manner, from intra-TAD regions. Such changes not only provide a molecular explanation to the weakening of intra-TAD interactions, but also support the notion that defective cohesin loop extrusion inside TADs releases this chromatin to engage in long-distance associations (Fig. 6e). Indeed, chromatin in infected cells displayed a higher frequency of extremely long-distance intra-chromosomal and inter-chromosomal interactions (Fig. 1e and Extended Data Fig. 2h). Consistent with this idea, genetic depletion of cohesin induced gains in long-distance chromatin interactions, supporting the idea that active loop extrusion counteracts chromatin mixing[3,12,13].

Importantly, host chromatin alterations resonate with the dichotomic deregulation of immune gene expression in COVID-19: weakened IFN responses accompany increased PIF gene expression[25]. Weakening of enhancer–promoter contacts and reduced enhancer activity correlate with inhibited IFN gene transcription, and CRISPRi data supported the regulatory roles of virus-weakened enhancers. These changes take place at critical loci, including *DDX58* (coding for virus sensor RIG-I) whose inhibition is required for successful infection[36]. Unexpectedly, SARS-CoV-2 infection selectively modifies the H3K4me3 of PIF gene promoters, suggesting unappreciated mechanisms at these promoters that confer aberrant inflammation in COVID-19 (ref. [25]). Additional discussion on the roles of cohesin, chromatin interactions and gene transcription, and limitations of this study can be found in the Supplementary Note.

Epigenetic alteration is known to exert long-term effects on gene expression and phenotypes[37,38]. Given the increasingly realized high incidence of post-acute SARS-CoV-2 sequelae (long COVID[39]), understanding the viral impacts on host chromatin and epigenome will not only provide new strategies to fight SARS-CoV-2 in the acute phase, but also pave the way for unravelling the molecular basis of long COVID for its intervention.

Methods

Cell culture

Human lung adenocarcinoma cells A549 expressing human ACE2 (A549-ACE2, NR-53821) were acquired from BEI Resources.

Fig. 5 | Chromatin restructuring and transcriptional inhibition of interferon response genes. a, Boxplots showing fold changes in RNA Pol2 (the RPB1 subunit) ChIP-seq for IFN (*n* = 40) and PIF genes (*n* = 12) due to infection (24 hpi, 0.1 MOI) or IFN-β treatment (1,000 U ml⁻¹, 6 h). *P* values were calculated using two-sided Mann–Whitney *U* test. For boxplots, the centre lines represent medians; box limits indicate the 25th and 75th percentiles; and whiskers extend 1.5 times the IQR from the 25th and 75th percentiles. **b**, Hi-C matrices (top) (bin size, 5 kb) and ChIP-seq for indicated factors at the *IFIT* gene cluster (bottom). Top right: mock. Lower left: SARS-CoV-2. Cyan arrows denote reduced dot-shaped loops. White lines mark the TAD, with intra-TAD interactions weakened throughout. Red asterisks show virus-reduced H3K27ac peaks. Black arrows show unchanged H3K4me3 peaks on *IFIT1/3* promoters. Colour scale indicates Hi-C contact frequencies. **c**, A diagram showing the ABC model of gene transcriptional outputs based on its enhancer activity and enhancer–promoter (E–P) contacts; ABC-P or ABC-P² are revised ABC algorithms considering promoter strength. **d**, A scatterplot showing the correlation between the ABC scores (*x* axis) and true transcriptional changes (*y* axis, SARS-CoV-2/Mock RPB1 ChIP-seq). Error bands (light cyan) indicate the 95% confidence interval of the regression estimate. Pearson's correlation coefficient is indicated. **e**, Top: CRISPRi/gRNAs that target the weakened enhancers in *IFIT* locus (red asterisks). The three enhancers were

numerically named for simplicity. Bottom: RT–qPCR showing how CRISPRi inhibition of enhancers affects *IFIT* gene induction in response to poly(I:C). gRNA1 and gRNA2 are two gRNAs targeting the same enhancer. *IFIT1* gene: from left to right, *P* = 0.0012, 0.0005, 0.0051, 0.0006 and 0.0004; *IFIT3* gene: from left to right, *P* = 0.0019, 0.0042, 0.0116, 0.0018 and 0.0016. Data are normalized to the -poly(I:C) in the control group and are presented as mean ± s.d. *n* = 3, representative of 2 independent experiments. *P* values were calculated using a two-sided independent *t*-test. **f**, Top left: experimental design and western blots showing acute RAD21 depletion and IFN-β treatment in RAD21-mAID HCT116 cells[27]. Alpha-tubulin served as a loading control and was run on the same membrane. Other barplots are RT–qPCR results of several IFN genes in indicated conditions. Veh: vehicle (without IAA). IAA: 5-ph-IAA (an auxin to induce RAD21 degradation). *P* = 2.97 × 10⁻⁶ (*IFIH1*), *P* = 0.0125 (*IFIT1*), *P* = 3.73 × 10⁻⁶ (*IFIT2*), *P* = 8.32 × 10⁻⁴ (*IFIT3*). *n* = 3, representative of two independent experiments. Data are presented as mean ± s.d. *P* values were calculated using a two-sided independent *t*-test. **g**, In the same region as **b**, Hi-C (top) (bin size, 5 kb) and ChIP-seq tracks for indicated factors at the *IFIT* gene cluster (bottom) after HCoV-OC43 infection. Top right: mock. Lower left: HCoV-OC43. The arrows and asterisks point to the same positions as in **b**. Colour scale indicates Hi-C contact frequencies.

They were maintained in DMEM/F-12 (1:1, Corning) medium supplemented with 10% FBS (GeneDepot) and blasticidin (100 μM). Normal A549 cells were purchased from ATCC (CCL-185) and cultured in DMEM/F-12 (1:1, Corning) supplemented with 10% FBS. 293T cells were from ATCC and were cultured in DMEM with 10% FBS. HCT-8 cells were purchased from ATCC (CCL-224) and cultured in RPMI 1640 with
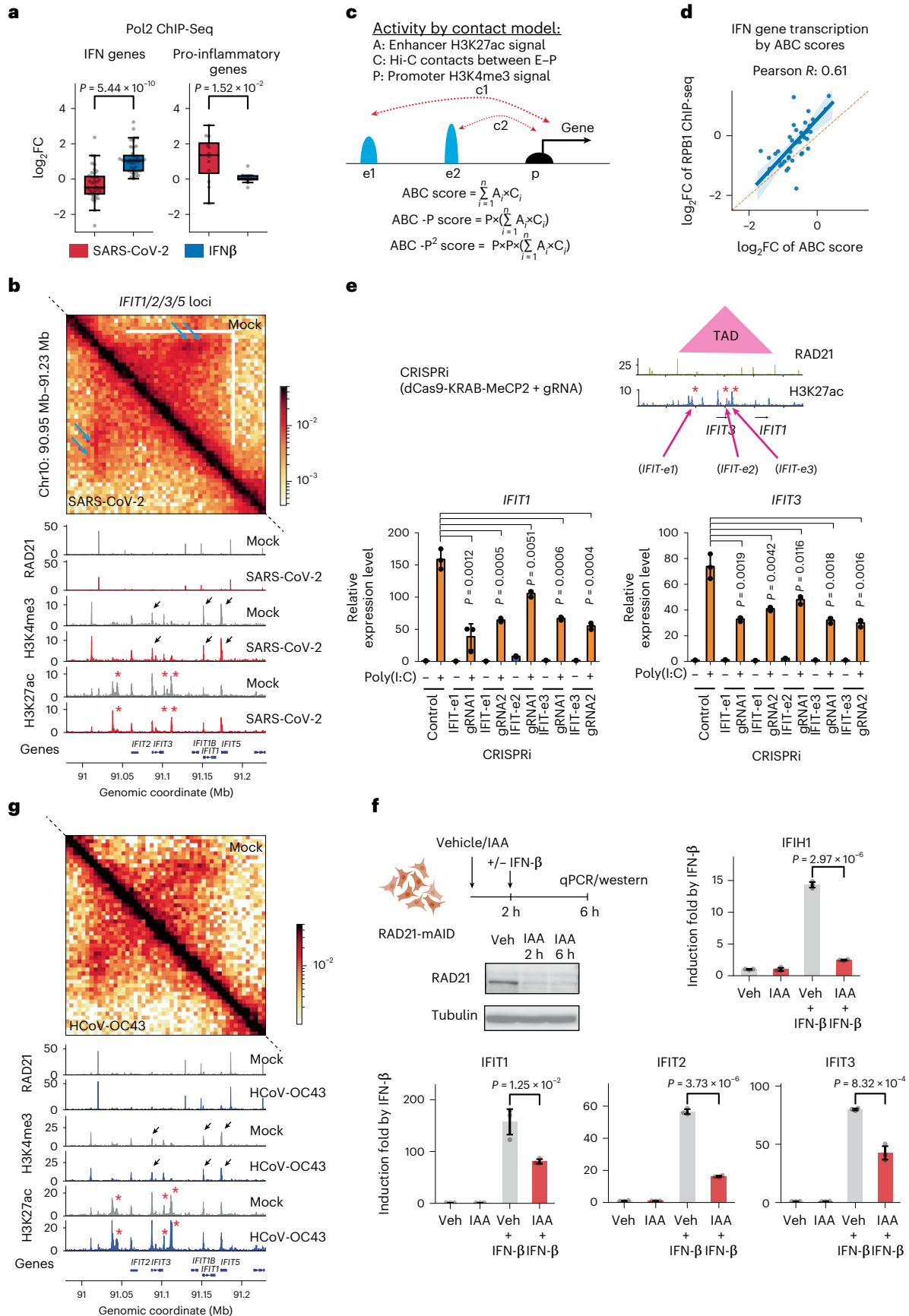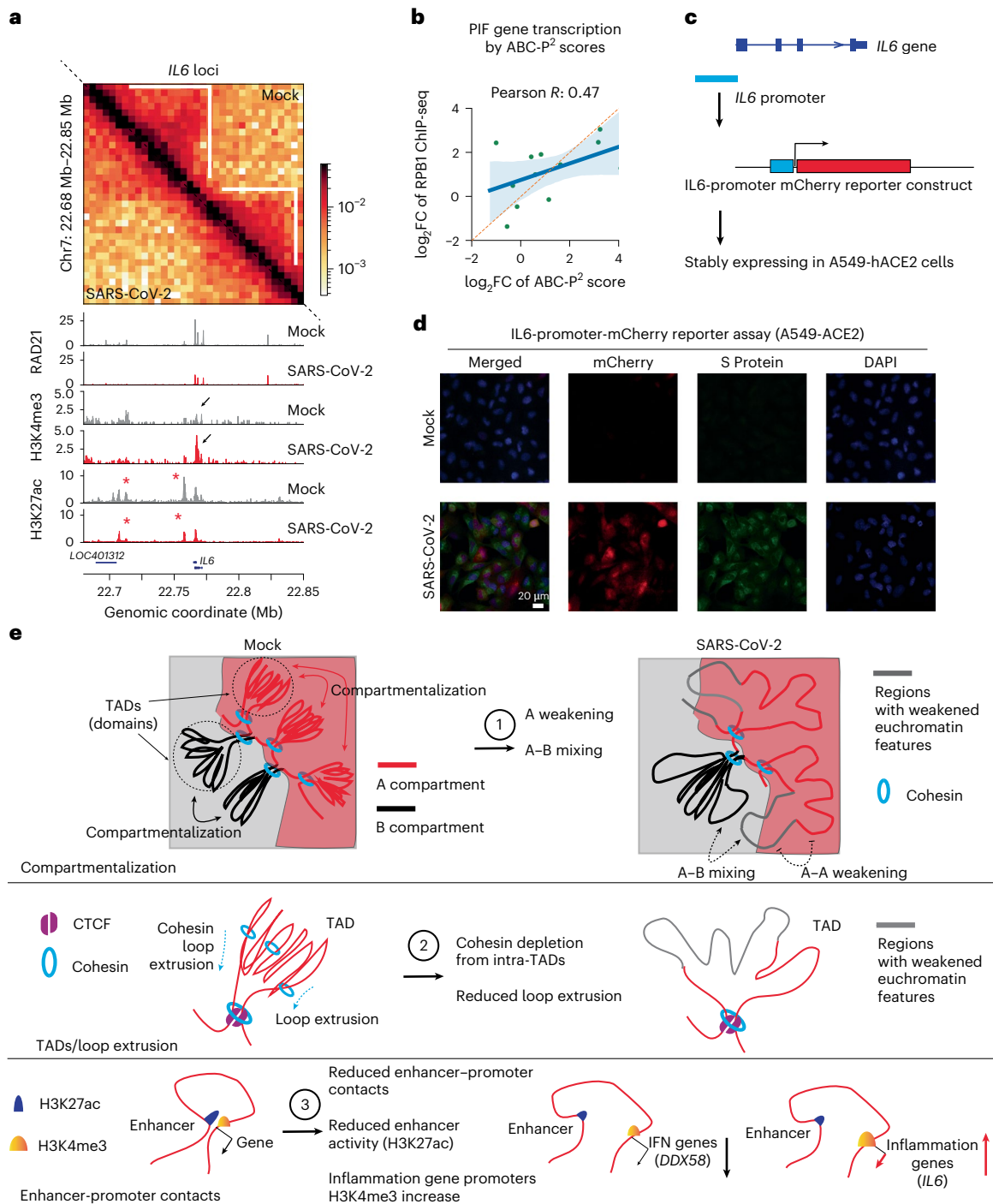
Fig. 6 | Augmented promoter H3K4me3 and pro-inflammatory gene activation. a, Hi-C matrices (top) (bin size, 5 kb) and ChIP-seq tracks at the *IL6* locus (bottom) in mock and SARS-CoV-2 conditions. White lines mark TADs, with intra-TAD interactions weakened throughout. Red asterisks show reduced H3K27ac peaks. Black arrows show enhanced H3K4me3 on *IL6* promoter. Colour scale indicates Hi-C contact frequencies. **b**, A scatterplot showing the correlation between the ABC-P² scores and true transcriptional changes in PIF genes (RPB1 ChIP-seq). Fold changes denote SARS-CoV-2/Mock. Error bands indicate the 95% confidence interval of the regression estimate. Pearson's correlation coefficient is shown. **c**, Diagram of an IL6-promoter-driven mCherry reporter.

d, Representative images of mCherry (red) and SARS-CoV-2 spike (S) protein (green) in cells carrying *IL6*-promoter-mCherry reporter under Mock or SARS-CoV-2 infection (0.1 MOI, 24 hpi). DAPI (blue). **e**, A model summarizing current observations of chromatin restructuring by SARS-CoV-2 infection at the 3D genome and epigenome scale. They are categorized from top to bottom in terms of A/B compartments, TADs/loop extrusion and enhancer–promoter contacts (see Extended Data Fig. 1a,b for additional information). These chromatin changes correlate with and may explain transcriptional deregulation of immuno-pathological gene deregulation in COVID-19 patients.

Transfection of plasmids or small interfering RNAs was performed using Lipofectamine 3000 or RNAiMAX (Life Technologies) following the manufacturer's instructions. For CRISPRi experiments, to examine enhancer functions during cell responses to RNA virus, we introduced polyinosinic:polycytidylic acid (poly (I:C), 333 ng ml^{-1}, Sigma, P9582) into A549 cells using lipofectamine 2000 and collected the total cellular RNAs for gene expression experiments after 4 h. For some experiments, fluorescein-labelled poly (I:C) was acquired from Invivogen (tlrl-picf). For the Hi-C 3.0 experiment, we introduced 66 ng ml^{-1} of poly (I:C) for 6 h to mimic RNA virus infection in the A549-ACE2 cell line. For interferon-beta (IFN-β) treatment, we treated A549-ACE2 cells with 1,000 U ml^{-1} recombinant human interferon beta (8499-IF-010/CF, R&D systems) for 6 h. For RAD21-mAID2-mClover cells, we first pre-treated cells wth 1 μM 5-ph-IAA for 2 h and then administered 1,000 U ml^{-1} interferon beta together with 1 μM 5-ph-IAA for 4 h.

SARS-CoV-2 and HCoV-OC43 infections in A549-ACE2 cells
SARS-CoV-2 isolate USA-WA1/2020 (NR-52281, BEI Resources) was used to infect human A549-ACE2 cells (NR-53821, BEI Resources). For viral infections, serum/antibiotics-free Eagle's MEM medium supplemented with 1 mM HEPES was used. Briefly, cells grown in 10-cm culture dishes at about 70–80% confluency were washed with the serum-free medium, and viral inoculum was added at 0.1 MOI for 1 h. Subsequently, non-adsorbed viral particles were gently aspirated out and the monolayers were replenished with 10% FBS containing MEM supplemented with 1 mM HEPES. Infected cells were incubated at 37 °C with 5% CO$_2$ for 6 h or 24 h post-infection for experiments. For heat-inactivated SARS-CoV-2 treatment, we treated the equivalent number of heat-inactivated virus (BEI resources, NR-52286) to 0.1 MOI on the basis of genomic equivalence (GE). Heat-inactivated SARS-CoV-2 (HI-WA1) was obtained from BEI Resources (NR-52286) and had 5.36×10^8 genome equivalents per ml. Heat-inactivated SARS-CoV-2 was given to cells using the same protocol as described above for SARS-CoV-2 isolate USA-WA1/2020 (NR-52281, BEI Resources), with the equivalent amount of 0.1 MOI based on GE.

HCoV-OC43 (VR-1558) was purchased from ATCC. For viral infections, serum/antibiotics-free RPMI 1640 medium was used. Briefly, A549-ACE2 cells grown in 10-cm culture dishes at about 80–90% confluency were washed two times with phosphate-buffered saline (PBS). Viruses were inoculated onto A549-ACE2 cells and allowed to adsorb for 2 h at 33 °C and 0.5 MOI. Then, non-adsorbed viral particles were gently aspirated out and the monolayers were replenished with 2% horse serum containing RPMI 1640. Infected cells were incubated at 33 °C with 5% CO$_2$ for 24 h post-infection for experiments.

Preparation of SARS-CoV-2 and HCoV-OC43 stock
The stock SARS-CoV-2 was propagated in Vero-E6 cells. Briefly, Vero-E6 cells were grown to 80% confluence in 10% FBS containing MEM medium supplemented with 1 mM HEPES and 1X antibiotics and antimycotics. Before infection, Vero-E6 cells were washed once with PBS, the viral inoculum was added to the flask in the presence of 3 ml of serum-free and antibiotics-free MEM medium supplemented with 1 mM HEPES, and the cells incubated for 1 h at 37 °C with 5% CO$_2$. At the end of incubation, non-adsorbed virus was aspirated out and cells were replenished with 25 ml of MEM supplemented with 10% FBS and 1 mM HEPES. Infected cells were incubated for 48 h at 37 °C with 5% CO$_2$. At 80% of cell lysis, SARS-CoV-2 was collected by detaching all the cells with a cell scraper and centrifuging at 300 g for 3 min. Viral aliquots were stored in screw-cap vials at −80 °C.

The stock of HCoV-OC43 was propagated in HCT-8 cells. Briefly, HCT-8 cells were grown to 80% confluence in RPMI 1640 medium containing 10% FBS. Before infection, HCT-8 cells were washed two times with PBS, the viral inoculum was added to the flask in the presence of 3 ml of serum-free and antibiotics-free RPMI 1640 and the cells incubated for 2 h at 33 °C with 5% CO$_2$. At the end of incubation, non-adsorbed virus was aspirated out and cells were replenished with 25 ml of RPMI 1640 supplemented with 2% horse serum. Infected cells were incubated for 5 d at 33 °C with 5% CO$_2$. At 80% of cell lysis, HCoV-OC43 was collected by detaching all the cells with a cell scraper and centrifuging at 300 g for 3 min. Viral aliquots were stored in screw-cap vials at −80 °C.

Determination of plaque forming units (p.f.u. ml^{-1} stock)
For the determination of infectious viral titres, plaque assays were performed using Vero-E6 cells. Briefly, Vero-E6 cells grown in 6-well plates were infected with 12 serial dilutions (1:10) of the SARS-CoV-2 stock in serum/BSA/antibiotic-free MEM medium with 1 mM HEPES for 1 h at 37 °C with 5% CO$_2$. At the end of incubation, non-adsorbed viral particles were aspirated and the infected cells were layered on MEM medium containing 0.5% agarose, 2% BSA and 1 mM HEPES, and incubated for 48 h at 37 °C with 5% CO$_2$. Fixation was carried out using 3.75% buffered formaldehyde (in PBS) for 10 min. After aspirating formaldehyde, the agarose layers were gently removed. Infected cells were stained with 0.3% crystal violet for 5 min, followed by washing once with PBS. Plates were air-dried and visible infectious plaques were counted in each dilution to determine the plaque forming units per millilitre of the stock.

To determine infectious viral particles for HCoV-OC43, the median tissue culture infectious dose (TCID$_{50}$) was determined using HCT-8 cells as follows: HCT-8 cells were seeded into 96-well plates at a concentration of 5×10^4 cells per well and incubated for 24 h to reach a confluence of 90%. Viral stock was serially diluted in RPMI 1640 containing 10% FBS in the range 10^{-1} to 10^{-8}.

Diluted viral samples were incubated at 33 °C for 5 d. Next, the medium was removed and replaced with 0.3% crystal violet for 5 min, followed by washing once with PBS. Wells were scored for the presence or absence of visual cytopathic effect in each dilution. The TCID$_{50}$ per millilitre was calculated by the Karber method[40]. For comparison to plaque assay results, TCID$_{50}$ per millilitre values were converted to p.f.u. per millilitre by multiplying by 0.7.

Lentiviral transduction and CRISPRi
We in-house generated a lentiviral construct expressing dCas9-KRAB-MeCP2 by PCR amplification of the dCas9-KRAB-MeCP2 (contains a domain of MeCP2) from pB-CAGGS-dCas9-KRAB-MeCP2 (Addgene, 110824), and then inserted it to the pLenti-EF1a-dCas9-VP64-2A-Blast backbone (Addgene, 61425) to replace the dCas9-VP64. The guide RNAs (gRNAs) used in CRISPRi were cloned into the Addgene 61427 backbone using BsmBI enzyme. To generate lentivirus, 293T cells were transfected with the lentiviral transfer vector DNA, psPAX2 packaging and pMD2.G envelope plasmid DNA at a ratio of 4:3:1 by lipofectamine 2000. After 16 h, the culturing medium was changed to a fresh one, and the supernatants were collected twice at 48 h and 72 h post-transfection. The collected lentiviral supernatants were filtered using 0.45 μm syringe filter (Thermo Fisher) and used to infect target A549 cells (polybrene (Sigma) was added at a final concentration of 8 μg ml^{-1}). To infect A549 cells for CRISPRi, cells were first infected by a lentivirus expressing dCas9-KRAB-MeCP2 for 24 h and selected with appropriate antibiotics (10 μg ml^{-1} blasticidin) for 7 d to generate a stable cell line. The stable cell line was then subjected to viral infection by individual gRNAs targeting each enhancer, and they were further selected with 100 μg ml^{-1} Zeocin for 4–7 d. These stable cells were then used for experiments. The gRNA cloning oligos are shown in Supplementary Table 2.

Promoter reporter assay
An *IL6* promoter-driven mCherry reporter construct was acquired from GeneCopoeia (HPRM30562-LvPM02). This lentiviral plasmid was introduced into the target cell line using lentiviral transduction similar to the steps described above in the lentivirus section. After 24 h of infection, the infected A549-ACE2 cells were selected under

2 µg ml⁻¹ puromycin. The established stable cell line was maintained in DMEM/F-12 (1:1, Corning) medium supplemented with 10% FBS (GeneDepot), 100 µg ml⁻¹ blasticidin and 2 µg ml⁻¹ puromycin. It was then used for Mock or SARS-CoV-2 infection (0.1 MOI, 24 hpi), and mCherry expression was examined by confocal imaging.

RNA extraction and RT–qPCR

RNA extraction of SARS-CoV-2-infected A549-ACE2 cells was performed by TRIzol (Thermo Fisher, 15596-026) following the manufacturer's instructions. In some other cases, RNA extraction from cells expressing CRISPRi or other transfection were performed using Quick-RNA Miniprep kit (Zymo Research, 11-328). Reverse transcription was conducted by using Superscript IV first strand synthesis kit (Thermo Fisher, 18091050), and the random hexamer primer was often used to test the expression levels of target genes. Real-time qPCR (RT–qPCR) was performed using SsoAdvanced Universal SYBR Green Supermix (Bio-Rad, 172-5274). Primer sequences used in this study can be found in Supplementary Table 2. Relative gene expression was normalized to the internal control (18S RNA).

Western blots

Cells were lysed in RIPA (50 mM Tris, pH 7.4, 150 mM NaCl, 1 mM EDTA, 0.1% SDS, 1% NP-40, 0.5% sodium deoxycholate) with cOmplete Mini Protease Inhibitor Cocktail (Roche, 11836153001) on ice for 30 min. Lysates were sonicated in Qsonica 800R (25% amplitude, 3 min, 10 s on 20 s off interval) and centrifuged at 18,407 g. The supernatants were mixed with 2x Laemmli sample buffer (Bio-Rad) and boiled at 95 °C for 10 min. The boiled proteins were separated on 4%–15% SDS–PAGE gradient gels and transferred to LF PVDF membrane (Bio-Rad, 1620260). The membranes were blocked in 5% skim milk in TBST (20 mM Tris, 150 mM NaCl and 0.2% Tween-20 (w/v)) for 1 h and then briefly washed in TBST twice. Then, the membranes were incubated in TBST with primary antibodies (GAPDH (Proteintech, 60004-1, 1:2,000 dilution), alpha-tubulin (Sigma, T5168, 1:1,000 dilution), RAD21 (Abcam, Ab992, GR214359-10, 1:1,000 dilution), CTCF (Millipore, 07-729, 1:1,000 dilution), SMC3 (Abcam, Ab9263, GR466-7, 1:1,000 dilution), total histone H3 (Abcam, Ab1791, GR206754-1,1:2,000 dilution), H3K4me3 (Abcam, Ab8580, GR3264490-1, 1:2,000 dilution), H3K9me3 (Abcam, Ab8898, GR164977-4, 1:2,000 dilution), H3K27ac (Abcam, Ab4729, GR3357415-1, 1:2,000 dilution) and H3K27me3 (Cell Signaling Technology, 9733S, 19, 1:2,000 dilution)) at 4 °C overnight. After washing 3 times in TBST, the blots were incubated in TBST with secondary antibody (horseradish peroxidase (HRP)-conjugated antibody) for 1 h. After 6 times of washing in TBST, the blots were developed in a Bio-Rad ChemiDoc gel imaging system. The intensity of the bands was quantified using ImageJ. To quantify relative expression,

protein expression normalized by the intensity of the control protein was compared between infected and the Mock-treated samples. As described in the figure legends, loading controls were run on the same membrane, and sample processing controls were run on a separate membrane with the same amount of protein loaded from the same samples.

Immunofluorescence microscopy and terminal deoxynucleotidyl transferase dUTP nick end labelling assay

Expression of spike protein of SARS-CoV-2 was measured by immunofluorescence microscopy. A549-ACE2 cells seeded on glass slides were infected with SARS-CoV-2 at an MOI of 0.1. At 24 hpi, cells were fixed with 4% paraformaldehyde in PBS for 1 h at room temperature. The coverslips were washed with 0.1% BSA in 1x PBS (wash buffer) and blocked with 1% BSA with 0.3% Triton-X-100 in PBST (blocking buffer) for 45 min at room temperature. Cells were incubated with an antibody targeting the SARS-CoV-2 spike glycoprotein (1:500, Abcam, ab272504) or a monoclonal antibody targeting the HCoV-OC43 (1:200, EMD Millipore, MAB9012) diluted in the blocking buffer overnight at 4 °C.

Subsequently after washes, cells were incubated with secondary antibody diluted in blocking buffer for 1 h at room temperature, followed by incubation with 4,6-diamidino-2-phenylindole (Invitrogen, D1306) for 5 min at room temperature. Coverslips were mounted in antifade mounting medium (Thermo Fisher, TA-030-FM) and fluorescence images were recorded using a Leica confocal microscope or a Nikon A1R. To assess apoptotic dead cells in the virus-infected condition, we used Click-iT TUNEL Alexa Fluor Imaging assay (Invitrogen, C10245) following the manufacturer's instructions. As a positive control of the terminal deoxynucleotidyl transferase dUTP nick end labelling (TUNEL) assay, one sample was incubated in DNase I solution for 30 min at room temperature, again following the manufacturer's instructions.

Hi-C 3.0

Hi-C 3.0 was performed on the basis of a recent protocol[14], which was largely modified on the basis of in situ Hi-C[19]. Briefly, ~5 million SARS-CoV-2-infected A549-ACE2 cells were washed once with PBS to remove debris and dead cells, trypsinized off the culture plates, cross-linked using 1% formaldehyde for 10 min at room temperature and quenched with 0.75 M Tris–HCl pH 7.5 for 5 min. These cells were further cross-linked with 3 mM disuccinimidyl glutarate for 50 min and again quenched with 0.75 M Tris–HCl pH 7.5 for 5 min. Cross-linked cell pellets were washed with cold PBS, resuspended in 0.5 ml ice-cold Hi-C lysis buffer (10 mM Tris–HCl, pH 8.0; 10 mM NaCl, 0.2% NP-40 and protease inhibitor cocktail) and rotated at 4 °C for 30 min. Nuclei were washed once with 0.5 ml ice-cold Hi-C lysis buffer. After pelleting down the nuclei, 100 µl 0.5% SDS was used to resuspend and permeabilize the nuclei at 62 °C for 10 min. Then, 260 µl H₂0 and 50 µl 10% Triton-X-100 were added to quench the SDS at 37 °C for 15 min. Subsequently, enzyme digestion of chromatin was performed at 37 °C overnight by adding an additional 50 µl of 10X NEB buffer 2, MboI (NEB, R0147M, 100U) and DdeI (NEB, R0175L, 100 U). After overnight incubation, the restriction enzyme was inactivated at 62 °C for 20 min. To fill in the DNA overhangs and add biotin, 35 U DNA polymerase I (Klenow, NEB, M0210) together with 10 µl 1 mM biotin-dATP (Jeana Bioscience) and 1 µl 10 mM dCTP/dGTP/dTTP were added and incubated at 37 °C for 1 h with rotation. Blunt-end Hi-C DNA ligation was performed using 5000 U NEB T4 DNA ligase with 10X NEB T4 ligase buffer (10 mM ATP, 90 µl 10% Triton X-100 and 2.2 µl 50 mg ml⁻¹ BSA) at room temperature for 4 h with rotation. After ligation, nuclei were pelleted down, resuspended with 440 µl Hi-C nuclear lysis buffer (50 mM Tris–HCl, pH 7.5, 10 mM EDTA, 1% SDS and protease inhibitor cocktail) and further sheared by a QSonica 800R sonicator using the parameters 10/20 s ON/OFF cycle, 25% Amp and 4 min. Around 10% of the sonicated chromatin was subjected to overnight decrosslinking at 65 °C, proteinase K treatment and DNA extraction. After DNA extraction, biotin labelled Hi-C 3.0 DNAs were purified using 20 µl Dynabeads MyOne Streptavidin C1 beads (Thermo Fisher, 65002). The biotinylated DNA on C1 beads was used to perform on-beads library making with NEBNext Ultra II DNA Library Prep kit for Illumina (NEB, E7645L) following the manufacturer's instructions. The sequencing was done on a NextSeq 550 platform with PE40 mode and demultiplexed with bcl2fastq v2.2.

ChIP-seq and spike-in calibrated ChIP-seq

ChIP-seq was performed as previously described with minor modifications[41]. For most ChIP-seqs in A549-ACE2 cells with Mock treatment or 24 h SARS-CoV-2 infection, ~5–10% of mouse ESCs (F121-9, a gift from David Gilbert) were added as spike-in controls before sonication with equal proportions to the two human cell samples (Extended Data Fig. 6a). For cell cross-linking for ChIP-seq, briefly, the cells were trypsinized in trypsin-EDTA (or Accutase for mESCs). After centrifugation, the cells were cross-linked with 1% formaldehyde in PBS for 10 min. The fixation steps were stopped in a quenching solution (0.75 M Tris–HCl pH 7.5) for 10 min. After centrifugation of the cells, we extracted the nuclei first using buffer LB1 (50 mM HEPES-KOH (pH 7.5), 140 mM NaCl,

1 mM EDTA (pH 8.0), 10% (v/v) glycerol, 0.5% NP-40, 0.25% Triton X-100 and 1× cocktail protease inhibitor), and then LB2 (10 mM Tris–HCl (pH 8.0), 200 mM NaCl, 1 mM EDTA (pH 8.0), 0.5 mM EGTA (pH 8.0) and 1× cocktail protease inhibitor). After centrifugation, the nuclei were suspended in buffer LB3 (10 mM Tris–HCl (pH 8.0), 100 mM NaCl, 1 mM EDTA (pH 8.0), 0.5 mM EGTA (pH 8.0), 0.1% Na-deoxycholate, 0.5% N-lauroyl sarcosine and 1× cocktail protease inhibitor) and the chromatin was fragmented with the Q800R3 sonicator (QSonica) using conditions of 10 s ON, 20 s OFF for 7–9 min (at 20% amplitude). Sheared chromatins were collected by centrifugation and incubated with appropriate antibodies (often 2–3 μg) at 4 °C overnight. The next morning, the antibody-protein-chromatin complex was retrieved by adding 25 μl pre-washed Protein G Dynabeads (Thermo Fisher, 10004D). Immunoprecipitated chromatin DNA was decrosslinked by heating at 65 °C overnight using elution buffer (1% SDS, 0.1 M NaHCO$_3$), treated with RNase A and proteinase K, and finally purified with phenol chloroform. The DNAs were subjected to sequencing library construction using NEBNext Ultra II DNA Library Prep kit for Illumina (NEB, E7645L) and deep sequenced on a NextSeq 550 platform using 40 nt/40 nt pair-ended mode. The antibodies used for ChIP-seq include RNA Polymerase II (RPB1 N terminus, Cell Signaling Technology, 14958S, 4), RAD21 (Abcam, Ab992, GR214359-10), SMC3 (Abcam, Ab9263, GR466-7), CTCF (Millipore, 07-729), NIPBL (Bethyl, A301-779A, 4), H3K4me3 (Abcam, Ab8580, GR3264490-1), H3K9me3 (Abcam, Ab8898, GR164977-4), H3K27ac (Abcam, Ab4729, GR3357415-1), H3K27me3 (Cell Signaling Technology, 9733S, 19) and HA (Abcam, Ab9110, GR3231414-3).

Ribo-depleted total RNA-seq
Total RNAs from mock or virus-infected A549-ACE2 cells were extracted with TRIzol, and 100–200 ng of total RNAs were used for making strand-specific ribosome-RNA-depleted sequencing library with the NEB Ultra II Directional RNA Library kit (E7760L) following the manufacturer's instructions. Libraries were sequenced on a NextSeq 550 using 40 nt/40 nt pair-ended mode.

Bioinformatic analyses
Calibrated ChIP-seq analyses. Sequencing reads were aligned to a concatenated genome of hg19 human genome assembly and mm9 mouse genome assembly with STAR (v2.7.0)[42]. Duplicated reads were removed, and only unique aligned reads were considered for later visualization and quantification. The scaling factor was calculated as the ratio of the number of reads uniquely aligned to human chromosomes versus the number of reads aligned to mouse chromosomes (Extended Data Fig. 6a). Uniquely aligned human reads were extracted with samtools (v1.9)[43] and normalized by the corresponding scaling factor with deeptools (v3.1.3)[44]. For RPB1 ChIP-seq gene transcription quantification, hg19 RefSeq gene annotation coordinates were used. The peak calling of most ChIP-seq was performed with the parameters -f BAM -q 0.01 in MACS2 (v2.1.4)[45]. Peaks with log$_2$ fold change of normalized ChIP-seq reads ratio smaller than −1 or greater than 1 were considered as reduced or gained peaks, respectively. ChIP-seq reads are summarized in Supplementary Table 1. A public NIPBL ChIP-seq dataset was obtained from SRR3102878.

RNA-seq analysis. RNA-seq reads were aligned to the hg19 reference human genome or SARS-CoV-2 viral genome (NC_045512.2) with STAR (v2.7.0)[42]. The percentage of reads uniquely aligned to SARS-CoV-2 genome versus total reads was calculated to verify a high viral infection rate. For human gene quantification, only uniquely aligned reads mapped to the hg19 genome were kept for further analysis.

Hi-C 3.0 data processing. Hi-C 3.0 raw data were primarily processed with Hi-C-Pro (v2.11.4)[46]. The pairs of reads were mapped to the human reference genome assembly hg19, and multimapped pairs, duplicated pairs and other unvalid 3C pairs were filtered out following the standard procedure of Hi-C-Pro. All valid Hi-C pairs were merged between replicates (unless specifically noted), and were further converted to Juicebox format[47] or cooler format[48] for visualization and further analyses. Hi-C contact matrices were normalized with 'cooler' (v0.8.11) 'balance' function. Read numbers of Hi-C are listed in Supplementary Table 1. The stratum-adjusted correlation coefficients (SCC) between two replicates were calculated to assess the reproducibility of Hi-C experiments[49]. The P(s) curve was calculated as a function of contact frequency (P) and genomic distances (s) (Fig. 1e). Only intra-chromosomal pairs (*cis*) were used to calculate the P(s) curve.

A/B compartment analyses. A/B nuclear compartments were identified on the basis of decomposed eigenvectors (E1) from 20 kb or 100 kb Hi-C contact matrices using cooltools (v0.4.1). A/B compartmental scores (E1) were corrected by GC densities in each bin. Saddle plot analyses were performed to measure the compartmentalization strength on a genome-wide scale using cooltools compute-saddle (similar to previous work[10,13]). Briefly, we first sorted the rows and columns in order of increasing compartmental scores within observed/expected (O/E) contact maps on the basis of data in Mock cells. Then we aggregated the rows and columns of the resulting matrix into 50 equally sized aggregate bins, and plotted the aggregated observed/expected Hi-C matrices as the 'saddle' plots (Fig. 3a). In Fig. 1c and elsewhere, Pearson correlation Hi-C matrices were used to emphasize the compartmental checkerboard pattern. We first calculated the observed/expected Hi-C maps as O/E matrices (bin size, 80,000 bp). Each value (*i*,*j*) in Pearson matrices indicates the Pearson correlation coefficient between the *i*-th column and the *j*-th column of O/E matrices (bin size, 80,000 bp). For changes in compartmental strength (Fig. 2c, and Extended Data Figs. 4a and 5a–c), the changes for each genomic region between Mock and SARS-CoV-2 samples were identified on the basis of 100-kb-binned compartmental scores (E1) of two Hi-C 3.0 replicates, largely following a previous study[20]. For each 100 kb, a Student's t-test was first performed on Mock and SARS-CoV-2 compartmental scores (E1). Only the 100 kb bins that have |delta E1| > 0.2 and P-value < 0.05 were considered as bins with changed compartmental strength. Different categories of compartment changes (in Fig. 2c) were defined as (similar to ref. [20]): A to stronger A: (Mock E1 - SARS-CoV-2 E1) < −0.2, Mock E1 > 0.2; B to A: (Mock E1 - SARS-CoV-2 E1) < −0.2, Mock E1 < −0.2, SARS-CoV-2 E1 > 0; B to weaker B: (Mock E1 - SARS-CoV-2 E1) < −0.2, Mock E1 < −0.2, SARS-CoV-2 E1 < 0; B to stronger B: (Mock E1 - SARS-CoV-2 E1) > 0.2, Mock E1 < −0.2; A to B: (Mock E1 - SARS-CoV-2 E1) < −0.2, Mock E1 > 0.2, SARS-CoV-2 E1 < 0; A to weaker A: (Mock E1 - SARS-CoV-2 E1) < −0.2, Mock E1 > 0.2, SARS-CoV-2 E1 > 0. For enrichment of epigenetic features on affected compartments (for example, see Fig. 2f), we ranked all 100 kb bins into six categories (top 5%, top 5–10%, 10–50%, 50–90%, bottom 5–10%, bottom 5%) and then calculated epigenomic features at each 100 kb bin. For histone modifications or chromatin regulatory factors that have sharp peaks in ChIP-seq (such as H3K27ac and H3K4me3), we quantified the numbers of peaks in each 100 kb bin. For modifications or factors that have broad ChIP-seq patterns (such as H3K9me3 and H3K27me3), we quantified the calibrated ChIP-seq reads throughout the entire 100 kb bin. The enrichment of these ChIP-seq signals was calculated by dividing the median quantification inside these six categories by the genome-wide median quantification.

TADs and insulation scores. Hi-C 3.0 data were used to identify TADs in A549-ACE2 cells following standard 4D Nucleome consortium protocol (github.com/4dn-dcic/docker-4dn-insulation-scores-and-boundaries-caller). First, insulation scores[22] and boundary strengths of each 10 kb bin with a 200 kb window size were measured to quantify the TAD insulation using cooltools (https://github.com/open2c/cooltools/blob/master/cooltools/cli/diamond_insulation.py). Then, we identified TAD boundaries in Mock and SARS-CoV-2-infected samples by using a boundary score cut-off of 0.5. We further merged

TAD boundaries identified in these two conditions and compared insulation scores at merged TAD boundaries (Fig. 4d). Merged TAD coordinates were used to perform downstream analyses. For each TAD, we quantified its mean Hi-C contacts throughout the domain (excluding very short distant interactions <15 kb), which we considered intra-TAD interaction in this paper. On the basis of the $\log_2$ fold changes of intra-TAD mean Hi-C contacts (SARS-CoV-2/Mock), we ranked all TADs into six categories (top 5%, top 5–10%, 10–50%, 50–90%, bottom 5–10%, bottom 5%) and calculated different epigenomic features of these six categories. For histone modifications or chromatin regulatory factors that have sharp peaks in ChIP-seq (such as H3K27ac, H3K4me3, CTCF or cohesin subunits), we quantified the numbers of peaks as well as the numbers of gained or lost peaks in different TADs. For modifications or factors that have broad ChIP-seq patterns (such as H3K9me3 and H3K27me3), we quantified the calibrated ChIP-seq reads throughout the TADs. The enrichment of these ChIP-seq signals was calculated by dividing the median quantification inside these six categories by the genome-wide median quantification.

Chromatin loop calling and enhancer–promoter contacts. For loop calling, we largely followed a recent 4DN benchmarking paper[14]. In brief, we used a reimplement of HICCUPS loop-calling tool, call-dots function inside cooltools (https://github.com/open2c/cooltools/blob/master/cooltools/cli/call_dots.py), to identify structural chromatin loops in different samples. We first called loops at 5 kb and 10 kb resolution separately, then used the following strategy to merge 5 kb and 10 kb loops. The 5 kb loops called at both 10 kb and 5 kb resolutions were first kept, all unique 10 kb resolution loops were kept, and only unique 5 kb loops smaller than 100 kb were kept. Differential loops were identified by first quantifying the Hi-C raw contacts at 40 kb resolution of each called loop, and then performing DESeq2 (v1.26.0)[50] differential analyses on these raw counts. We considered loops with a DESeq2 FDR < 0.1 and a $\log_2 FC > 0$ or <0 as virus-strengthened or weakened chromatin loops. The APA was performed by superimposing observed/expected Hi-C matrices on merged loops with the coolpuppy tool (v0.9.2)[51].

ABC score. ABC score calculation largely followed a previous study[26] with modifications. For the A score (enhancer activity) of a gene, we first identified all putative enhancers of this gene by selecting H3K27ac ChIP-seq peaks located within 1 Mb of the promoter. Then we quantified the calibrated H3K27ac ChIP-seq signals on these putative enhancers (extended 150 bp from MACS2 peaks) as A scores. The A-only quantification of enhancer activity for this gene would be the sum of the A scores for all putative enhancers. For the C score (enhancer–promoter contact) between a gene and putative enhancers, we quantified the normalized Hi-C contacts formed in between the 5 kb bins harbouring the gene promoter and the putative enhancer. For the ABC score, we multiplied the A score of each enhancer by the C score, and generated the summation of these if multiple putative enhancers exist for a gene. The P score of any gene was calculated as the calibrated H3K4me3 ChIP-seq signal at its promoter region (±2.5 kb from transcription start site). For ABC-P or ABC-P^2 scores, we multiplied the summed ABC score of a gene by its P score (promoter H3K4me3 signal) or by the square of its P score. The transcriptional changes of any gene were calculated on the basis of the $\log_2$ fold change of RPB1 ChIP-seq reads over the whole gene body (average of three ChIP-seq replicates). Pearson correlation coefficient was used to measure the correlation between ABC score change and transcriptional change. The list of IFN response genes was obtained from GSEA molecular signature databases (Interfero_Alpha_Response), and the list of PIF genes was manually curated on the basis of recent literature[52] studying immuno-pathology of SARS-CoV-2 infection (see Supplementary Table 3).

Statistics. For all boxplots, the centre lines represent medians; box limits indicate the 25th and 75th percentiles; and whiskers extend 1.5 times the interquartile range (IQR) from the 25th and 75th percentiles. For qPCR, data were analysed using Prism (v7.00) and presented as mean ± s.d., as indicated in figure legends. At least two biological replicates were conducted for RNA-seq, ChIP-seq or Hi-C sequencing. Student's t-test (two-tailed) was commonly used to compare means between two qPCR groups; $P < 0.05$ was considered significant (*$P < 0.05$; **$P < 0.01$; ***$P < 0.001$). Statistical analyses for sequencing data were performed with Python (v3.6, pandas v1.1.5, numpy v1.17.3, matplotlib v3.1.2, scipy v1.5.4) or R (v3.6.0) scripts.

Reporting summary
Further information on research design is available in the Nature Portfolio Reporting Summary linked to this article.

Data availability
Data generated in this study have been deposited to NCBI GEO (GSE179184, https://www.ncbi.nlm.nih.gov/geo/query/acc.cgi?acc=GSE179184). Raw data from fluorescence microscopy imaging are available at Mendeley (https://doi.org/10.17632/czzb4jb8ss.1). Gene sets are available from GSEA molecular signature database (https://www.gsea-msigdb.org/gsea/msigdb). Source data are provided with this paper.

Code availability
Key software or algorithms used in our analysis of sequencing data are listed in Methods, Hi-C data analyses tools can be found at https://github.com/open2c. This work did not report new software or mathematical algorithms.

References
1. Dekker, J., Marti-Renom, M. A. & Mirny, L. A. Exploring the three-dimensional organization of genomes: interpreting chromatin interaction data. *Nat. Rev. Genet.* **14**, 390–403 (2013).
2. Kempfer, R. & Pombo, A. Methods for mapping 3D chromosome architecture. *Nat. Rev. Genet.* **21**, 207–226 (2020).
3. Davidson, I. F. & Peters, J.-M. Genome folding through loop extrusion by SMC complexes. *Nat. Rev. Mol. Cell Biol.* https://doi.org/10.1038/s41580-021-00349-7 (2021).
4. Liu, X. et al. Human virus transcriptional regulators. *Cell* **182**, 24–37 (2020).
5. Heinz, S. et al. Transcription elongation can affect genome 3D structure. *Cell* **174**, 1522–1536.e22 (2018).
6. Tsai, K. & Cullen, B. R. Epigenetic and epitranscriptomic regulation of viral replication. *Nat. Rev. Microbiol.* **18**, 559–570 (2020).
7. Kee, J. et al. SARS-CoV-2 disrupts host epigenetic regulation via histone mimicry. *Nature* **610**, 381–388 (2022).
8. Gordon, D. E. et al. A SARS-CoV-2 protein interaction map reveals targets for drug repurposing. *Nature* **583**, 459–468 (2020).
9. Mirny, L. A., Imakaev, M. & Abdennur, N. Two major mechanisms of chromosome organization. *Curr. Opin. Cell Biol.* **58**, 142–152 (2019).
10. Belaghzal, H. et al. Liquid chromatin Hi-C characterizes compartment-dependent chromatin interaction dynamics. *Nat. Genet.* **53**, 367–378 (2021).
11. Hildebrand, E. M. & Dekker, J. Mechanisms and functions of chromosome compartmentalization. *Trends Biochem. Sci.* **45**, 385–396 (2020).
12. Rao, S. S. P. et al. Cohesin loss eliminates all loop domains. *Cell* **171**, 305–320.e24 (2017).
13. Schwarzer, W. et al. Two independent modes of chromatin organization revealed by cohesin removal. *Nature* **551**, 51–56 (2017).
14. Oksuz, B. A. et al. Systematic evaluation of chromosome conformation capture assays. *Nat. Methods* **18**, 1046–1055 (2021).

15. Su, J.-H., Zheng, P., Kinrot, S. S., Bintu, B. & Zhuang, X. Genome-scale imaging of the 3D organization and transcriptional activity of chromatin. *Cell* **182**, 1641–1659.e26 (2020).

16. Gorbalenya, A. E. et al. The species *Severe acute respiratory syndrome-related coronavirus*: classifying 2019-nCoV and naming it SARS-CoV-2. *Nat. Microbiol.* **5**, 536–544 (2020).

17. Zhao, X. et al. Interferon induction of IFITM proteins promotes infection by human coronavirus OC43. *Proc. Natl Acad. Sci. USA* **111**, 6756–6761 (2014).

18. Humphries, F. et al. A diamidobenzimidazole STING agonist protects against SARS-CoV-2 infection. *Sci. Immunol.* **6**, eabi9002 (2021).

19. Rao, S. S. P. et al. A 3D map of the human genome at kilobase resolution reveals principles of chromatin looping. *Cell* **159**, 1665–1680 (2014).

20. Yusufova, N. et al. Histone H1 loss drives lymphoma by disrupting 3D chromatin architecture. *Nature* **589**, 299–305 (2021).

21. Liu, N. Q. et al. WAPL maintains a cohesin loading cycle to preserve cell-type-specific distal gene regulation. *Nat. Genet.* **53**, 100–109 (2021).

22. Crane, E. et al. Condensin-driven remodelling of X chromosome topology during dosage compensation. *Nature* **523**, 240–244 (2015).

23. Zhang, H. et al. Chromatin structure dynamics during the mitosis-to-G1 phase transition. *Nature* **576**, 158–162 (2019).

24. Krietenstein, N. et al. Ultrastructural details of mammalian chromosome architecture. *Mol. Cell* **78**, 554–565.e7 (2020).

25. Carvalho, T., Krammer, F. & Iwasaki, A. The first 12 months of COVID-19: a timeline of immunological insights. *Nat. Rev. Immunol.* **21**, 245–256 (2021).

26. Fulco, C. P. et al. Activity-by-contact model of enhancer–promoter regulation from thousands of CRISPR perturbations. *Nat. Genet.* **51**, 1664–1669 (2019).

27. Yesbolatova, A. et al. The auxin-inducible degron 2 technology provides sharp degradation control in yeast, mammalian cells, and mice. *Nat. Commun.* **11**, 5701 (2020).

28. Cuartero, S. et al. Control of inducible gene expression links cohesin to hematopoietic progenitor self-renewal and differentiation. *Nat. Immunol.* **19**, 932–941 (2018).

29. Calderon, L. et al. Cohesin-dependence of neuronal gene expression relates to chromatin loop length. *eLife* **11**, e76539 (2022).

30. Rinaldi, L. et al. The glucocorticoid receptor associates with the cohesin loader NIPBL to promote long-range gene regulation. *Sci. Adv.* **8**, eabj8360 (2022).

31. Cano-Rodriguez, D. et al. Writing of H3K4Me3 overcomes epigenetic silencing in a sustained but context-dependent manner. *Nat. Commun.* **7**, 12284 (2016).

32. Policarpi, C., Munafo, M., Tsagkris, S., Carlini, V. & Hackett, J. A. Systematic epigenome editing captures the context-dependent instructive function of chromatin modifications. Preprint at *bioRxiv* https://doi.org/10.1101/2022.09.04.506519 (2022).

33. Ferreira-Gomes, M. et al. SARS-CoV-2 in severe COVID-19 induces a TGF-β-dominated chronic immune response that does not target itself. *Nat. Commun.* **12**, 1961 (2021).

34. Ho, J. S. Y. et al. TOP1 inhibition therapy protects against SARS-CoV-2-induced lethal inflammation. *Cell* **184**, 2618–2632.e17 (2021).

35. Zazhytska, M. et al. Non-cell-autonomous disruption of nuclear architecture as a potential cause of COVID-19-induced anosmia. *Cell* **185**, 1052–1064.e12 (2022).

36. Yamada, T. et al. RIG-I triggers a signaling-abortive anti-SARS-CoV-2 defense in human lung cells. *Nat. Immunol.* **22**, 820–828 (2021).

37. Cavalli, G. & Heard, E. Advances in epigenetics link genetics to the environment and disease. *Nature* **571**, 489–499 (2019).

38. Mantovani, A. & Netea, M. G. Trained innate immunity, epigenetics, and Covid-19. *N. Engl. J. Med.* **383**, 1078–1080 (2020).

39. Nalbandian, A. et al. Post-acute COVID-19 syndrome. *Nat. Med.* **27**, 601–615 (2021).

40. Kärber, G. Beitrag zur kollektiven Behandlung pharmakologischer Reihenversuche. *Naunyn Schmiedebergs Arch. Exp. Pathol. Pharmakol.* **162**, 480–483 (1931).

41. Lee, J.-H. et al. Enhancer RNA m6A methylation facilitates transcriptional condensate formation and gene activation. *Mol. Cell* **81**, 3368–3385.e9 (2021).

42. Dobin, A. et al. STAR: ultrafast universal RNA-seq aligner. *Bioinformatics* **29**, 15–21 (2013).

43. Li, H. et al. The Sequence Alignment/Map format and SAMtools. *Bioinformatics* **25**, 2078–2079 (2009).

44. Ramírez, F., Dündar, F., Diehl, S., Grüning, B. A. & Manke, T. deepTools: a flexible platform for exploring deep-sequencing data. *Nucleic Acids Res.* **42**, W187–W191 (2014).

45. Zhang, Y. et al. Model-based analysis of ChIP-seq (MACS). *Genome Biol.* **9**, R137 (2008).

46. Servant, N. et al. HiC-Pro: an optimized and flexible pipeline for Hi-C data processing. *Genome Biol.* **16**, 259 (2015).

47. Durand, N. C. et al. Juicer provides a one-click system for analyzing loop-resolution Hi-C experiments. *Cell Syst.* **3**, 95–98 (2016).

48. Abdennur, N. & Mirny, L. A. Cooler: scalable storage for Hi-C data and other genomically labeled arrays. *Bioinformatics* **36**, 311–316 (2020).

49. Yang, T. et al. HiCRep: assessing the reproducibility of Hi-C data using a stratum-adjusted correlation coefficient. *Genome Res.* **27**, 1939–1949 (2017).

50. Love, M. I., Huber, W. & Anders, S. Moderated estimation of fold change and dispersion for RNA-seq data with DESeq2. *Genome Biol.* **15**, 550 (2014).

51. Flyamer, I. M., Illingworth, R. S. & Bickmore, W. A. Coolpup. py: versatile pile-up analysis of Hi-C data. *Bioinformatics* **36**, 2980–2985 (2020).

52. Blanco-Melo, D. et al. Imbalanced host response to SARS-CoV-2 drives development of COVID-19. *Cell* **181**, 1036–1045.e9 (2020).

53. Ahn, J. H. et al. Phase separation drives aberrant chromatin looping and cancer development. *Nature* **595**, 591–595 (2021).

Acknowledgements

Competing interests

The authors declare no competing interests.

Additional information

Extended data is available for this paper at https://doi.org/10.1038/s41564-023-01344-8.

Supplementary information The online version contains supplementary material available at https://doi.org/10.1038/s41564-023-01344-8.

Correspondence and requests for materials should be addressed to Wenbo Li.

Peer review information *Nature Microbiology* thanks the anonymous reviewers for their contribution to the peer review of this work.
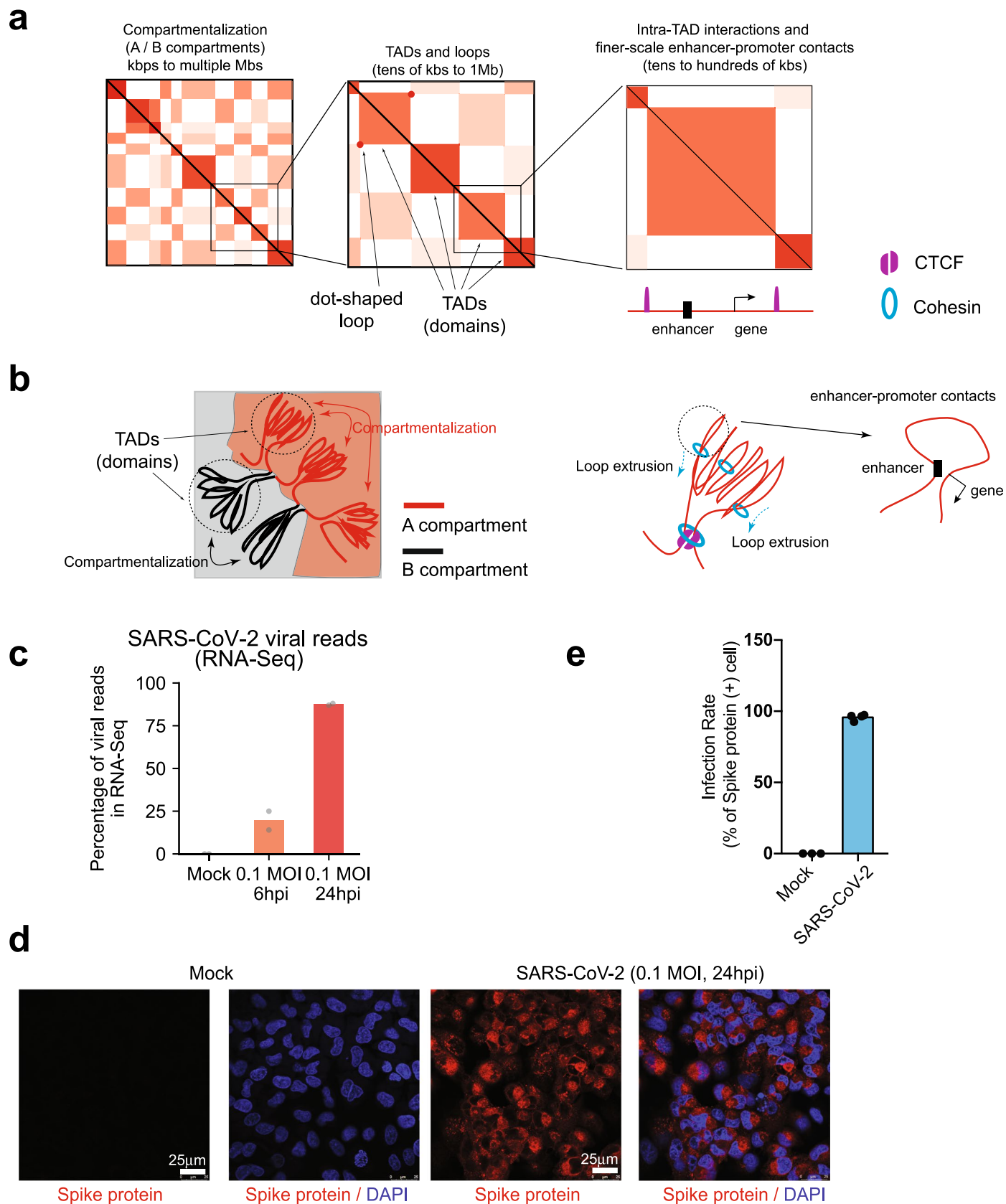
Reprints and permissions information is available at www.nature.com/reprints.

Publisher's note Springer Nature remains neutral with regard to jurisdictional claims in published maps and institutional affiliations.

Disclosure: The content is solely the responsibility of the authors and does not necessarily represent the official views of the Cancer Prevention and Research Institute of Texas.

a

Compartmentalization
(A / B compartments)
kbps to multiple Mbs

TADs and loops
(tens of kbs to 1Mb)

Intra-TAD interactions and
finer-scale enhancer-promoter contacts
(tens to hundreds of kbs)

dot-shaped loop

TADs (domains)

enhancer   gene

CTCF

Cohesin

b

TADs (domains)

Compartmentalization

Compartmentalization

A compartment

B compartment

enhancer-promoter contacts

Loop extrusion

Loop extrusion

enhancer

gene

c

SARS-CoV-2 viral reads
(RNA-Seq)

Percentage of viral reads in RNA-Seq

Mock   0.1 MOI 6hpi   0.1 MOI 24hpi

e

Infection Rate
(% of Spike protein (+) cell)

Mock   SARS-CoV-2

d

Mock

SARS-CoV-2 (0.1 MOI, 24hpi)

25μm

25μm

Spike protein   Spike protein / DAPI   Spike protein   Spike protein / DAPI

Extended Data Fig. 1 | See next page for caption.

Extended Data Fig. 1 | Overview of 3D chromatin architectures and quality control of SARS-CoV-2 infection in our study. a. A diagram showing the typical contact maps in Hi-C (and Hi-C 3.0 or other modified Hi-C approaches) that define A/B compartments, Topologically Associating Domains (TADs), chromatin loops or intra-TAD interactions (which perhaps include most enhancer-promoter contacts). This is an overall summary of these structures, but the exact definition of some structures may be subject to variable interpretation, and the terminology may not always be used consistently[2,3,9,19]. Often, A/B compartmentalization is illustrated by a checkerboard pattern of Hi-C contact matrices over large genomic sizes, indicating preferential interactions between genomic regions belonging to the same type of compartments (A: euchromatin and transcriptionally active; B: heterochromatin, transcriptionally inactive). TADs or chromatin domains are often characterized as a square or triangle-like structure on contact maps, reflecting a higher contact frequency between any regions inside the same TAD than with regions outside of the TAD. Intra-TAD enhancer-promoter contacts are considered to be facilitated by TADs, while TAD boundaries prevent aberrant interaction with regions outside of TADs. In Hi-C maps, the dot-shaped structures on the tip of domains suggests local enrichment of spatial interaction between a pair of two loci over nearby regions, and is regarded as a chromatin loop in this work. But loops may be subjected to other

definitions in other studies. For example, enhancer-promoter contacts often do not appear as dot-shaped structures in Hi-C, but may be defined as loops by other work or other methods. For additional discussion, see[2,9]. **b.** Cartoon diagrams describe A-A and B-B association preference within regions of similar epigenetic features, which compartmentalizes chromosomes into A and B (the left part of the diagram). The diagram in the middle depicts a current model of cohesin loop extrusion inside TADs that generates such structures. The right side shows a zoom-in view of a part of a TAD that harbors enhancer-promoter contact that may play roles in gene transcriptional regulation. **c.** A barplot showing the percentage of RNA-Seq reads mapped to SARS-CoV-2 genome in Mock, 6-hr post infection (6 hpi, 0.1 MOI), and 24 hpi (0.1 MOI) conditions (n = 2). Mean and standard deviation were calculated based on two biological replicates of RNA-Seq. This data is consistent with previous observations[52]. Shorter term infection for 6-hr resulted in ~20% RNA-Seq reads attributed to the virus genome, suggesting insufficient viral infection/replication in cell populations. **d.** Confocal images showing immunofluorescence staining of DAPI (DNA, blue) and the Spike protein of SARS-CoV-2 (red) in Mock and 24hpi (0.1 MOI) infected A549-ACE2 cells. Scale bars are shown. **e.** Quantification of infection rates in panel **d**. SARS-CoV-2 Spike protein was used as a marker for SARS-CoV-2 infection. From left to right, n = 3 and 4 quantifications.
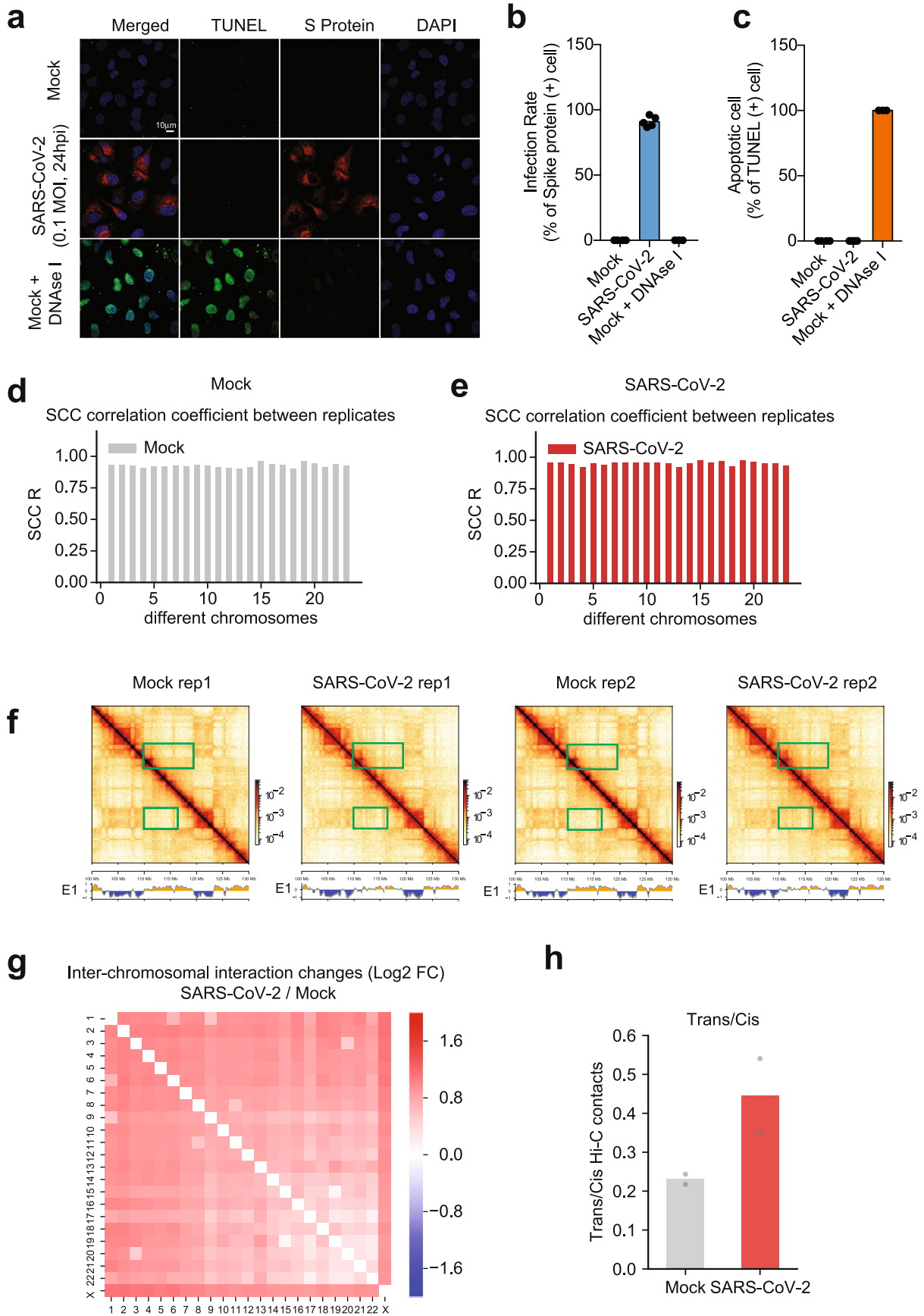
Extended Data Fig. 2 | See next page for caption.

**Extended Data Fig. 2 | Cell quality check after infection, replicate consistency of Hi-C 3.0, and the increase of trans-chromosomal interactions after infection. a**. Representative confocal images of Mock and SARS-CoV-2 infected cells (24hpi, 0.1 MOI) stained with an antibody against the Spike protein of SARS-CoV-2 (S protein, red), and by the TUNEL assay (green). **b,c**. Quantification of rates of apoptosis and infection from panel **a**. From left to right, quantifications were conducted n = 4, 5, 3 (for panel b) and n = 4, 5, 3 (for panel c). **d,e**. Barplots showing the SCC correlation coefficients[49] between two Hi-C replicates of Mock or SARS-CoV-2 conditions for different chromosomes. **f**. Snapshots showing two replicates of Hi-C contact matrices and compartment score (E1) tracks in the same genomic region shown in Fig. 1b. The left two matrices show data of replicate 1 (rep1), and the right two matrices show replicate 2 (rep2). Green boxes show two regions with increased A-B compartmental mixing or weakened A compartment after virus infection. Bin size = 80 kb. Color scales indicate Hi-C contact frequencies. **g**. A heatmap shows the log2 fold change of inter-chromosomal interactions between any two chromosomes (SARS-CoV-2/Mock). **h**. A barplot showing the trans/cis Hi-C contacts ratio in two biological replicates of Hi-C in Mock or SARS-CoV-2 infected cells (n = 2). Trans contacts indicate chromatin interactions formed in between two different chromosomes.
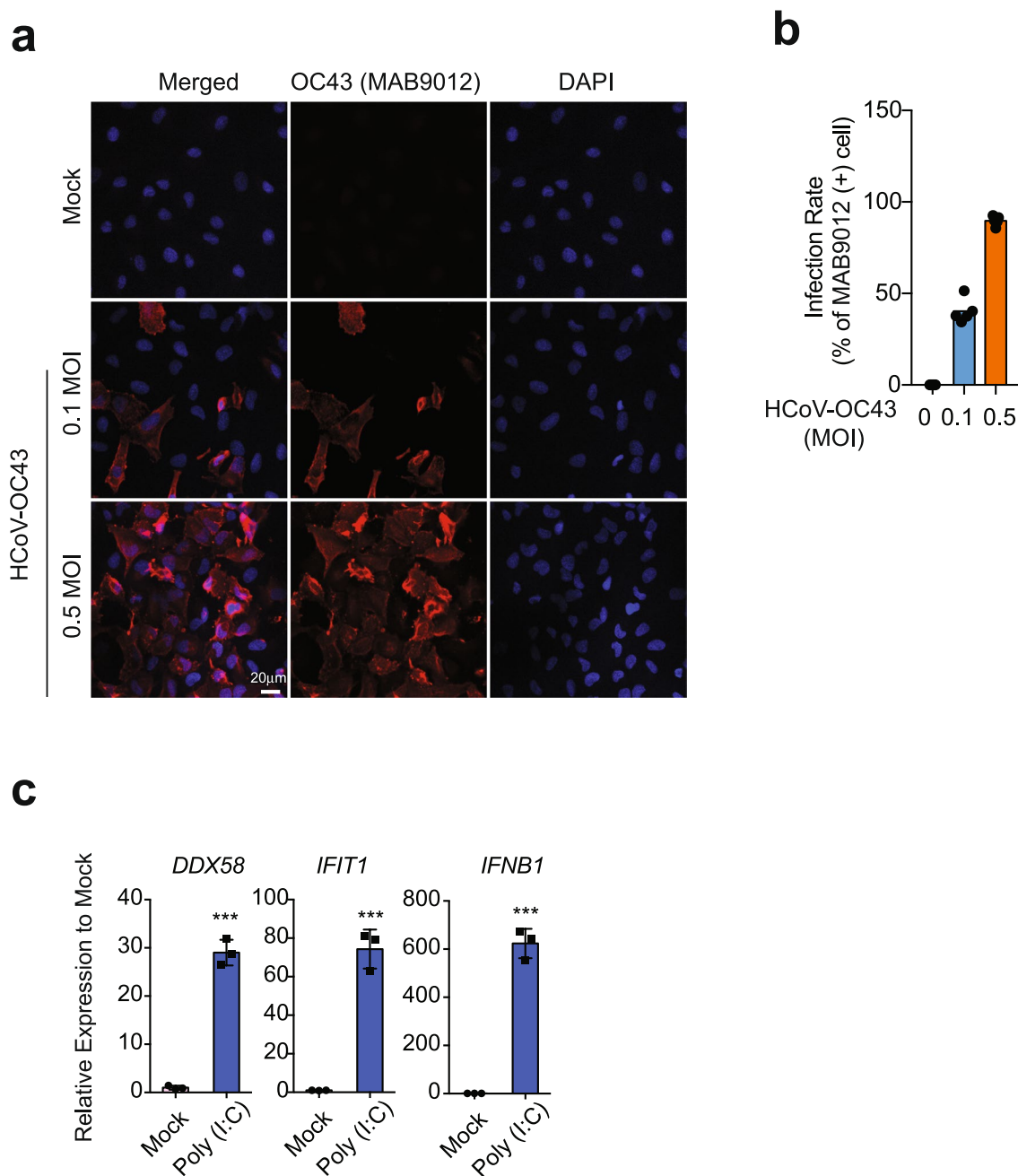
Extended Data Fig. 3 | Quality check of HCoV-OC43 infection and Poly (I:C) treatment in A549-ACE2 cells. a. To examine how many cells were infected by HCoV-OC43 at 24hpi, immunostaining using a monoclonal antibody targeting HCoV-OC43 was conducted (MAB9012). Here we show representative confocal images of Mock and HCoV-OC43 infected A549-ACE2 cells stained with MAB9012 (red) and DAPI (blue). Scale bar is shown. **b.** Barplots showing quantification of infection rates of HCoV-OC43 at 0.1 and 0.5 MOIs (24hpi). Data shows n = 5 for each quantification. **c.** Barplots of *DDX58*, *IFIT1*, *IFNB1* gene expression (RT-qPCR) showing known antiviral responses in poly(I:C) transfected cells. n = 3, representative of two independent experiments, P = 5.59e-5 (*DDX58*), 2.31e-4 (*IFIT1*), 5.94e-5 (*IFNB1*), calculated with a two-sided independent t-test. Data show Mean + /- SD from replicates (***, p < 0.001).
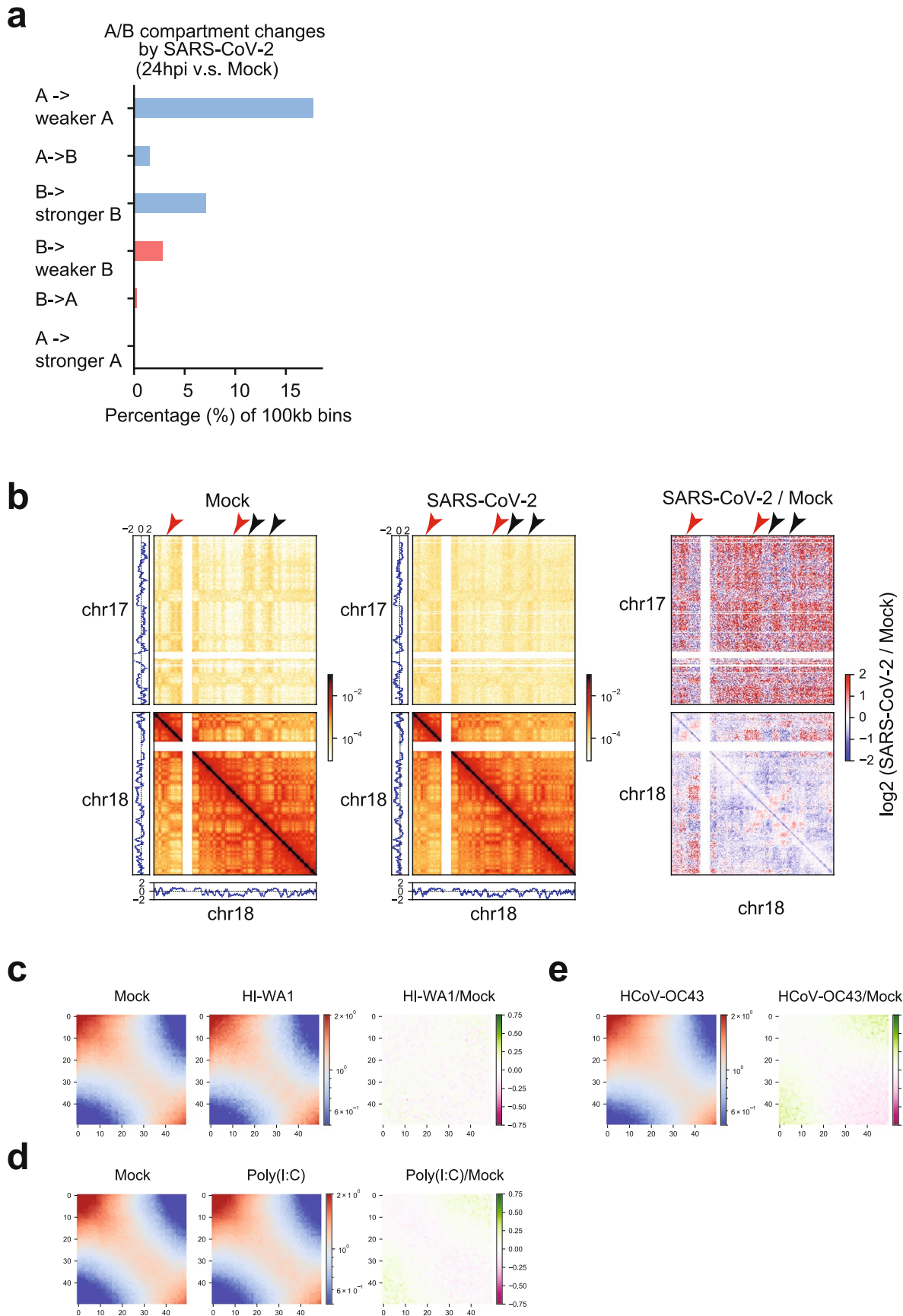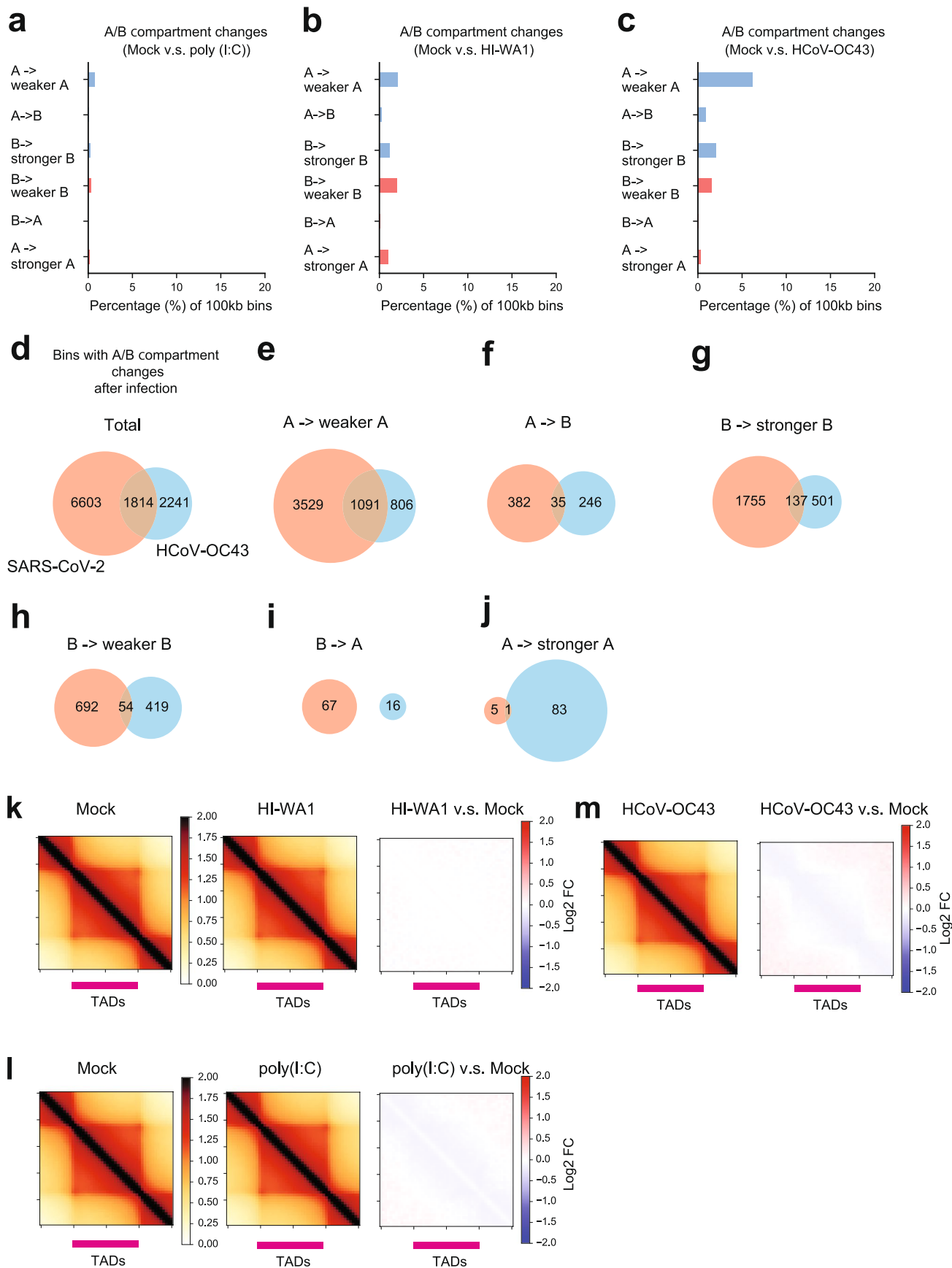
Extended Data Fig. 4 | See next page for caption.

Extended Data Fig. 4 | Additional data of A/B compartmental changes.
a. A barplot showing the percentage of genomic bins (100 kb bin size) that can be categorized into six groups based on their compartmental score changes after SARS-CoV-2 infection (E1 value change > 0.2, see Methods). These six categories are: A to weaker A, A to B, B to stronger B, B to weaker B, B to A, and A to stronger A. **b**. Snapshots of inter-chromosomal Hi-C contact matrices between chr17 and chr18 (upper), and intra-chromosomal Hi-C contact matrices within chr18 (lower) in Mock and SARS-CoV-2 infected samples. On the right, differential contacts are shown as log2 fold changes of SARS-CoV-2/Mock. PCA E1 scores were put at sides to show the A or B compartments. Red and black arrowheads respectively point to increased A-B and reduced A-A interactions after SARS-CoV-2 infection. Bin size = 320 kb. Color scales indicate Hi-C contact frequencies (left and middle), and log2 fold change of SARS-CoV-2/Mock contact frequencies (right). **c,d,e**. Saddle plots from Hi-C 3.0 after treatments by HI-WA1 (**c**), poly(I:C) (**d**), and HCoV-OC43 infection (**e**), respectively, showing negligible impacts on compartmental interactions. HCoV-OC43 and HI-WA1 shared the same Mock sample. In each figure, color scales indicate observed/expected (O/E) Hi-C contact frequencies (left and middle), and log2 fold change of O/E contact frequencies (right).

Extended Data Fig. 5 | See next page for caption.

Extended Data Fig. 5 | Limited 3D genome changes in cells infected by HCoV-OC43, treated by HI-WA1 or poly(I:C). a,b,c. Barplots showing the percentage of genomic bins (100 kb bin size) that can be categorized into six groups based on their compartmental score changes (E1 values). These six categories are: A to weaker A, A to B, B to stronger B, B to weaker B, B to A, and A to stronger A. The **a,b,c** panels show the changes after treatments by poly (I:C), HI-WA1 and HCoV-OC43, respectively. **d-j.** Venn diagrams showing the overlaps of genomic bins displaying E1 score alteration (that is, compartmental changes) incurred by SARS-CoV-2 (pink) versus those by HCoV-OC43 (Cyan). Numbers indicate bins with changes belong to different categories: total changed bins (**d**), A to weaker A(**e**), A to B (**f**), B to stronger B (**g**), B to weaker B(**h**), B to A(**i**), A to stronger A(**j**). **k-m.** Aggregated domain analyses (ADA) in cells treated by HI-WA1, poly(I:C) and HCoV-OC43, in comparison to their corresponding mock samples. HI-WA1 and HCoV-OC43 samples share the same Mock. In each figure, color scales indicate aggregated Hi-C contact frequencies (left and middle), and log2 fold change of SARS-CoV-2/Mock aggregated contact frequencies (right).
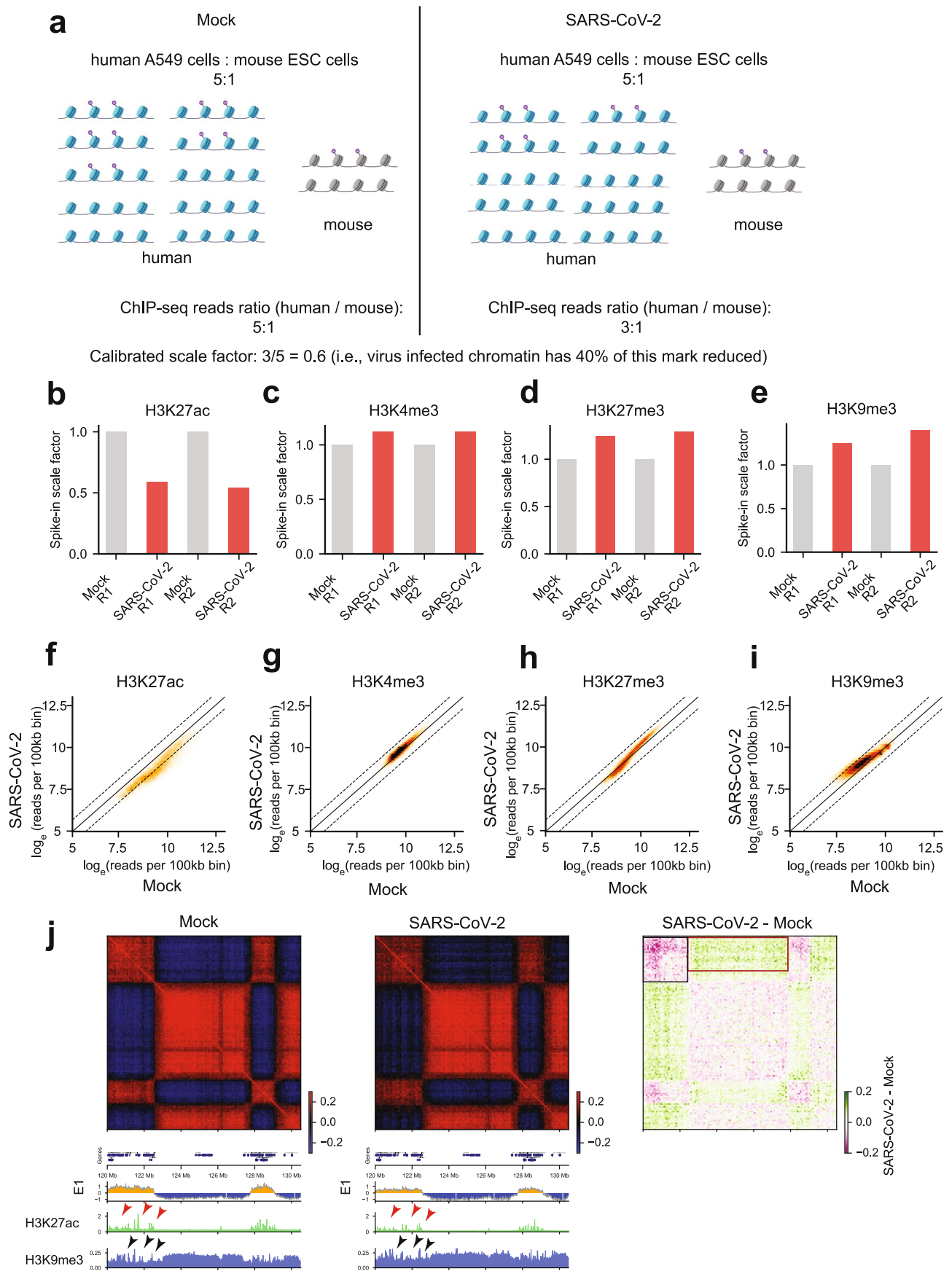
Extended Data Fig. 6 | See next page for caption.

Extended Data Fig. 6 | Calibrated ChIP-Seqs demonstrate epigenome reprogramming during SARS-CoV-2 infection. a. A diagram illustrating the design of calibrated ChIP-Seq using mouse ESCs as spike-in for human A549 cells (with or without infection). Created with BioRender.com. **b,c,d,e**. Barplots showing the scale factors calculated based on human/mouse reads in both Mock and SARS-CoV-2 conditions, which permit calibrated ChIP-Seq analyses of H3K27ac, H3K4me3, H3K27me3, and H3K9me3. R1 and R2 indicate biological replicates 1 and 2. **f,g,h,i**. Scatter plots show virus-caused genome-wide changes of histone mark ChIP-Seq signals at 100 kb bins for H3K27ac, H3K4me3, H3K9me3 and H3K27me3. The x,y-axis are natural logarithmically scaled reads densities from calibrated ChIP-Seq data. Dotted lines denote changes by two folds. **j**. Snapshots of Pearson's correlation matrices, E1 compartmental scores, as well as ChIP-Seq tracks of H3K27ac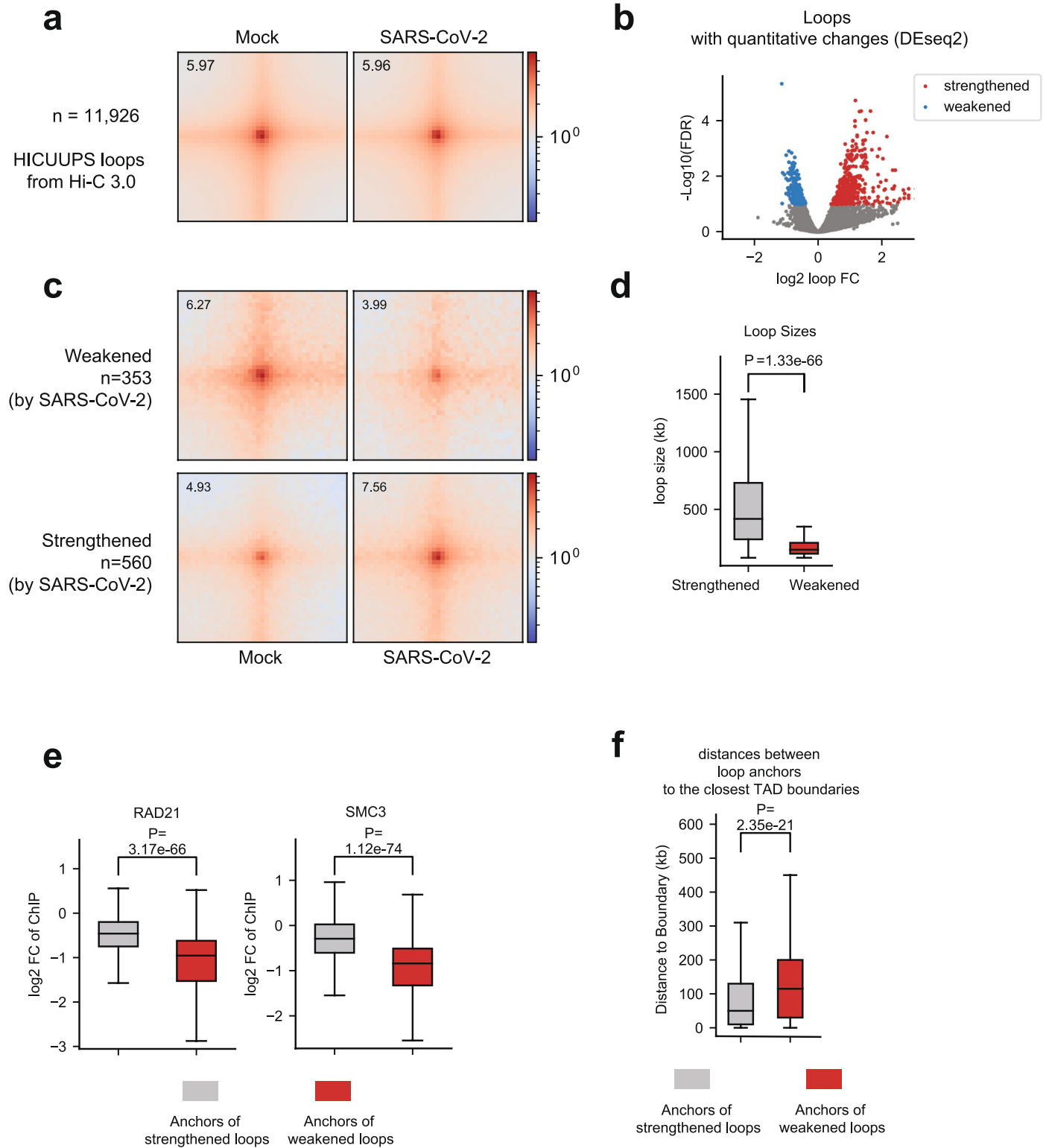 and H3K9me3 in Mock or SARS-CoV-2 infected cells. The right side shows the difference of Pearson's correlation matrices between SARS-CoV-2 and Mock (pink color shows decrease; green shows increase). At the bottom, red arrowheads on top of the H3K27ac peaks show strong reduction after infection, which was accompanied by quantitative increase of H3K9me3 signals in the same region (black arrowheads). Accordingly, this entire A compartment domain displays reduced compartmental strength (that is, lower PCA E1 scores, see yellow signals in the E1 track), showing less A-A compartmental interactions within the same A compartment (black box in the rightmost panel) and increased A-B mixing with the nearby B compartment (red box in the rightmost panel). Bin size = 80 kb. Color scales indicate Pearson correlation coefficient (left and middle), and the differences of Pearson correlation coefficient (right).
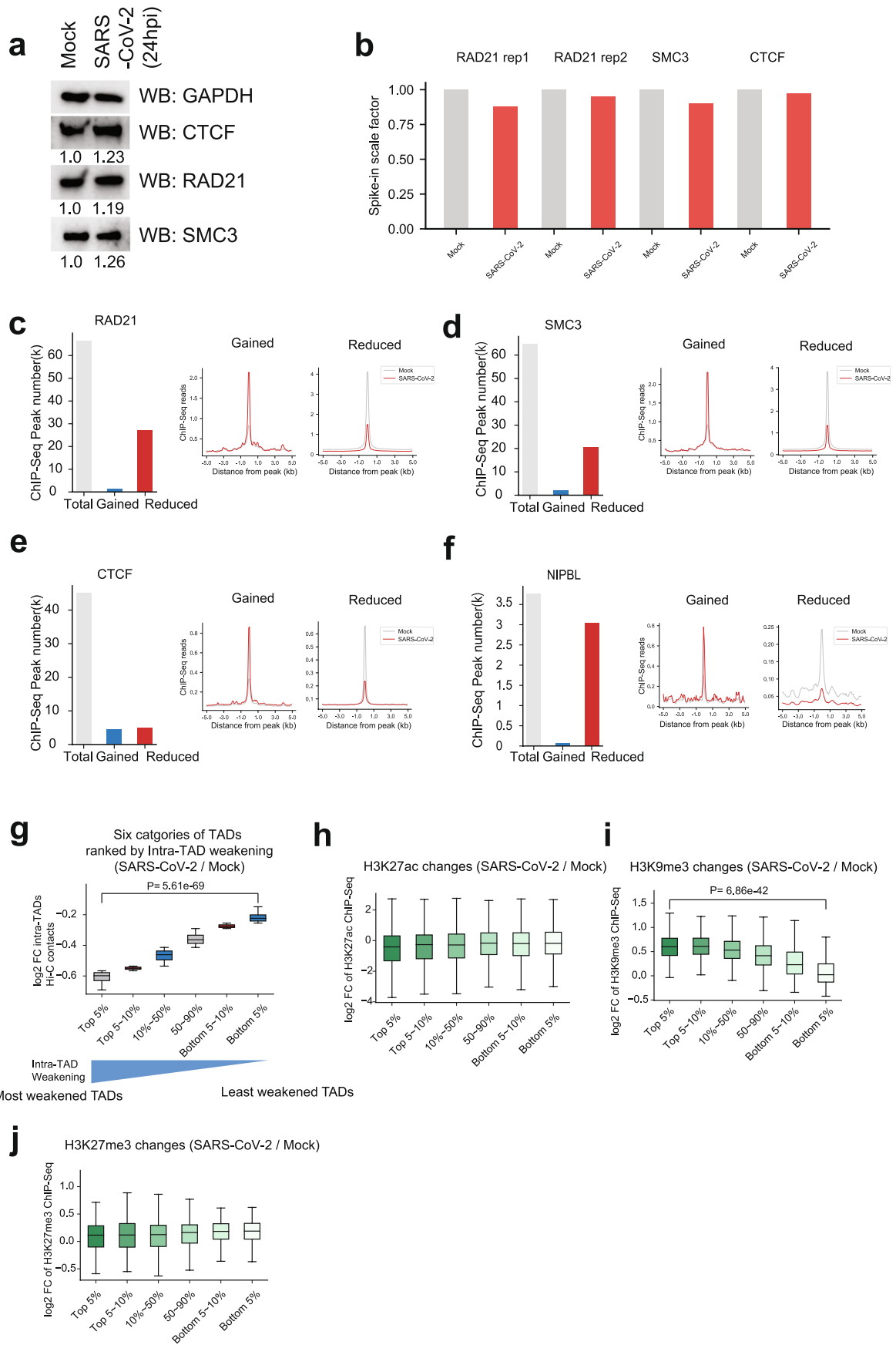
Extended Data Fig. 7 | See next page for caption.

Extended Data Fig. 7 | Cohesin was specifically depleted from intra-TAD regions and epigenetic features of different groups of TADs. a. Western blots showing the protein abundances of cohesin (RAD21, SMC3) and CTCF in Mock and SARS-CoV-2 infected cells. GAPDH was used as a loading control. Relative expression of each protein to the Mock control group was labelled under each image. **b**. Barplots showing the scale factors calculated based on human/mouse reads ratio in both Mock and SARS-CoV-2 conditions that permit calibrated ChIP-Seqs of CTCF, RAD21 and SMC3. These factors were not globally affected by virus infection (the ratios are comparable in mock and infected conditions). **c**. Left barplot shows the numbers of total, the gained or reduced RAD21 ChIP-Seq peaks after SARS-CoV-2 infection at 24hpi; the profile plots in the middle and right show the signals of RAD21 ChIP-Seq at the gained or reduced ChIP-Seq peaks in Mock and SARS-CoV-2 conditions. **d,e,f**. Similar to panel c, these plots show analysis of ChIP-seqs of SMC3, CTCF and NIPBL in Mock and SARS-CoV-2 conditions. **g**. A boxplot showing the log2 fold changes (FC) of intra-TAD Hi-C contacts for six categories of TADs. All TADs are ranked based on the quantitative changes of intra-TAD interactions and the six categories include the Top 5%, top 5-10%, 10-50%, 50-90%, bottom 5-10%, and the bottom 5%, respectively. "Top 5%" represents TADs with the most severely-weakened intra-TAD interactions after SARS-CoV-2 infection. From left to right, n = 205, 205, 1637, 1637, 205, 205 TADs. P = 5.61e-69, calculated with a two-sided Mann-Whitney U test. **h,i,j**. Boxplots showing the log2 fold changes (FC) of ChIP-Seq signals of H3K27ac (from left to right, n = 1808, 1841, 18640, 22245, 3074, 3205 peaks), H3K9me3 (from left to right, n = 205, 205, 1637, 1637, 205, 205 regions), and H3K27me3 (from left to right, n = 205, 205, 1637, 1637, 205, 205 regions) in the six categories of TADs as shown in panel **g**. P = 6.86e-42 in H3K9me3 panel, calculated with a two-sided Mann-Whitney U test. For all boxplots, the centre lines represent medians; box limits indicate the 25th and 75th percentiles; and whiskers extend 1.5 times the interquartile range (IQR) from the 25th and 75th percentiles.

a

Mock   SARS-CoV-2

n = 11,926

HICUUPS loops
from Hi-C 3.0

5.97   5.96

10^0

b

Loops
with quantitative changes (DEseq2)

- strengthened
- weakened

−Log10(FDR)

log2 loop FC

c

Weakened
n=353
(by SARS-CoV-2)

6.27   3.99

10^0

Strengthened
n=560
(by SARS-CoV-2)

4.93   7.56

10^0

Mock   SARS-CoV-2

d

Loop Sizes

P =1.33e-66

loop size (kb)

Strengthened   Weakened

e

RAD21
P=
3.17e-66

log2 FC of ChIP

SMC3
P=
1.12e-74

log2 FC of ChIP

Anchors of
strengthened loops

Anchors of
weakened loops

f

distances between
loop anchors
to the closest TAD boundaries

P=
2.35e-21

Distance to Boundary (kb)

Anchors of
strengthened loops

Anchors of
weakened loops

Extended Data Fig. 8 | See next page for caption.

Extended Data Fig. 8 | Dot-shaped chromatin loops are largely unaltered by SARS-CoV-2 infection, but a subset of them is changed. a. Aggregated peak analysis (APA) shows the strength of all chromatin loops (observed/expected) in Mock (left) and SARS-CoV-2 (right) infected cells for 11,926 dot-shaped loops called by call-dots algorithm. Color scales indicate aggregated Hi-C observed / expected (O/E) contacts. **b**. Volcano plot generated by DEseq2 using the two replicates of Hi-C that defines quantitatively changed loops after SARS-CoV-2 infection (FDR < 0.1, see Methods[53]). **c**. APA plots for the subsets of virus-weakened and strengthened loops. The numbers of such loops are shown. For APA plots in panels a and c, the bin size for plotting the heatmap is 5 kb, and the heatmaps show genomic regions +/- 100 kb surrounding the loop anchors. The numbers on the heatmaps indicate the central pixel values. Color scales indicate aggregated Hi-C O/E contacts. **d**. A boxplot showing the sizes of loops belonging to strengthened and weakened groups. From left to right, n = 560 and 353. P = 1.33e-66, calculated with a two-sided Mann-Whitney U test. **e**. Boxplots showing the virus-induced fold changes of cohesin binding (measured by calibrated cohesin ChIP-Seq) on the loop anchors of the two groups of loops: those quantitatively strengthened or weakened. From left to right, n = 983 and 535 (RAD21); from left to right, n = 1023 and 543 (SMC3). P = 3.17e-66 (RAD21). P = 1.12e-74 (SMC3). P-values are calculated with a two-sided Mann-Whitney U test. **f**. Boxplots showing the distances of each loop anchor to its closest TAD boundary for two groups of virus-affected loops: those quantitatively strengthened or weakened. From left to right, n = 1038 and 687. P = 2.35e-21, calculated with a two-sided Mann-Whitney U test. For all boxplots, the centre lines represent medians; box limits indicate the 25th and 75th percentiles; and whiskers extend 1.5 times the interquartile range (IQR) from the 25th and 75th percentiles.
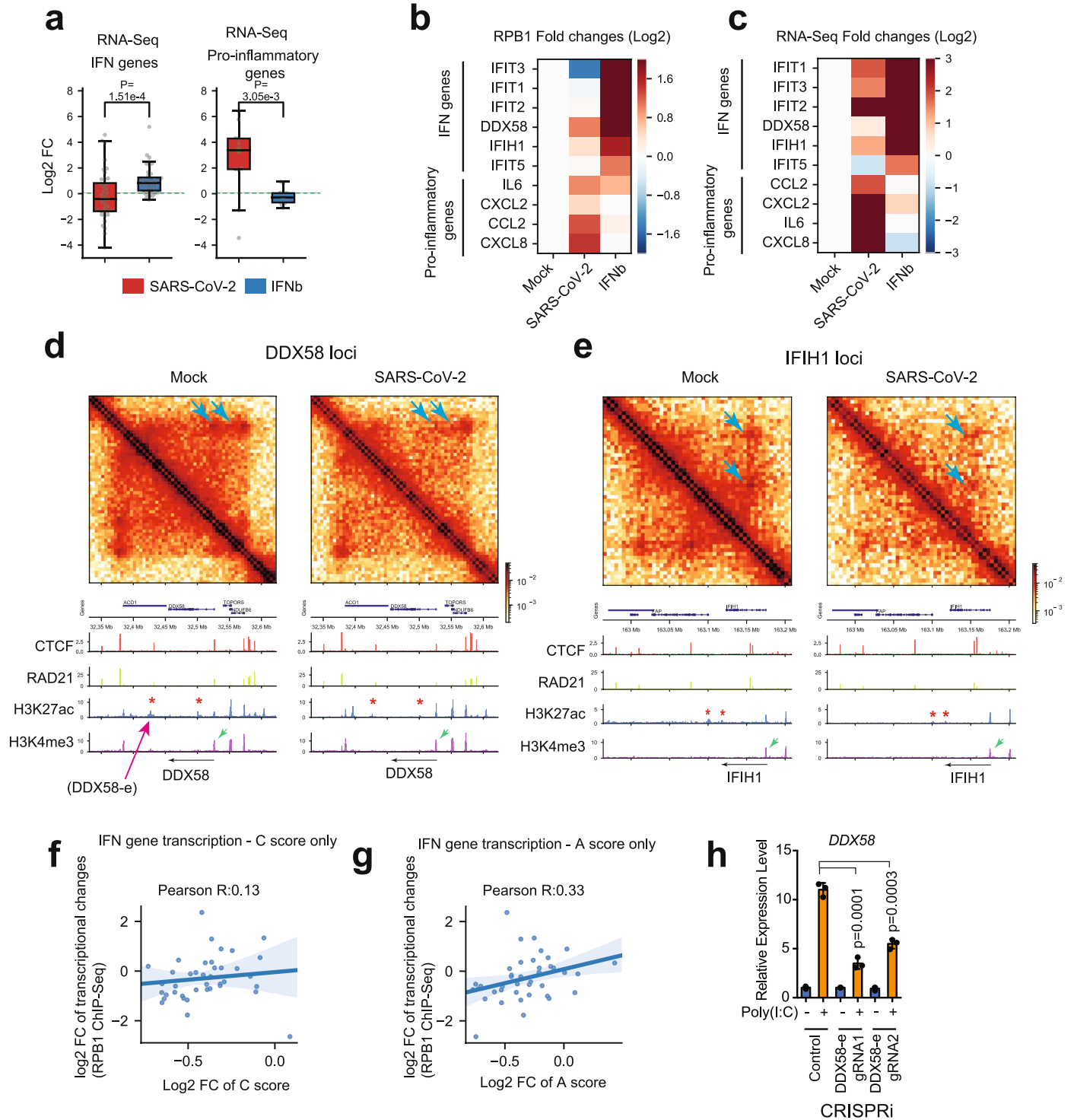
Extended Data Fig. 9 | See next page for caption.

Extended Data Fig. 9 | SARS-CoV-2 disruption of chromatin architecture correlates with the transcriptional inhibition of interferon response genes.
a. Boxplots showing the expression deregulation of key interferon response (IFN) (n = 40) and pro-inflammatory (PIF) genes (n = 12) after SARS-CoV-2 infection or IFN-beta treatment (1000 u/ml, 6-hr), as shown by RNA-Seq changes. P = 1.51e-4 and 3.05e-3, respectively, calculated with a two-sided Mann-Whitney U test. For boxplots, the centre lines represent medians; box limits indicate the 25th and 75th percentiles; and whiskers extend 1.5 times the interquartile range (IQR) from the 25th and 75th percentiles. **b,c.** Heatmaps of select IFN or PIF genes showing their fold changes in Pol2 ChIP-Seq or RNA-seq after SARS-CoV-2 infection or IFN-beta treatment (1000 u/ml, 6-hr). **d,e.** Hi-C matrices (bin size: 5 kb) and calibrated ChIP-Seq tracks for indicated factors at two key loci encoding viral RNA sensors: *DDX58* (encoding RIG-I) and *IFIH1* (encoding for MDA5). Left: Mock; right: SARS-CoV-2. Blue arrows point to reduced dot-shaped loops. The intra-TAD interactions were weakened throughout these two TADs. Red asterisks show reduced H3K27ac peaks by virus infection. Green arrows show H3K4me3 peaks at promoters that are not changed by SARS-CoV-2. A pink arrow in panel **d** points

to the enhancer targeted by CRISPRi in panel **h** (see below). Color scales indicate Hi-C contact frequencies. **f.** A scatter plot showing a poor correlation between the C score only (from Hi-C contact, x-axis) and the true transcriptional changes of IFN genes by SARS-CoV-2 (y-axis, RPB1 ChIP-Seq). Error bands indicate the 95% confidence interval of the regression estimate. Pearson's correlation coefficient for contact only: R = 0.13. X and y-axis fold changes denote SARS-CoV-2/Mock. **g.** Similar to panel f, this is a scatter plot showing a poor correlation between the A score only (from enhancer H3K27ac activity, x-axis) and the true transcriptional changes of IFN genes by SARS-CoV-2 (y-axis, RPB1 ChIP-Seq). Error bands indicate the 95% confidence interval of the regression estimate. Pearson's correlation coefficient for enhancer activity only: 0.33. **h.** RT-qPCR results showing that CRISPRi inhibition of the enhancer in *DDX58* locus reduced its response to poly (I:C). The *DDX58* enhancer for CRISPRi is shown in panel d. Data was normalized to the -poly(I:C) in control group, and denote mean +/- SD (n = 3, representative of two independent experiments); P values were calculated with a two-sided independent T-test.
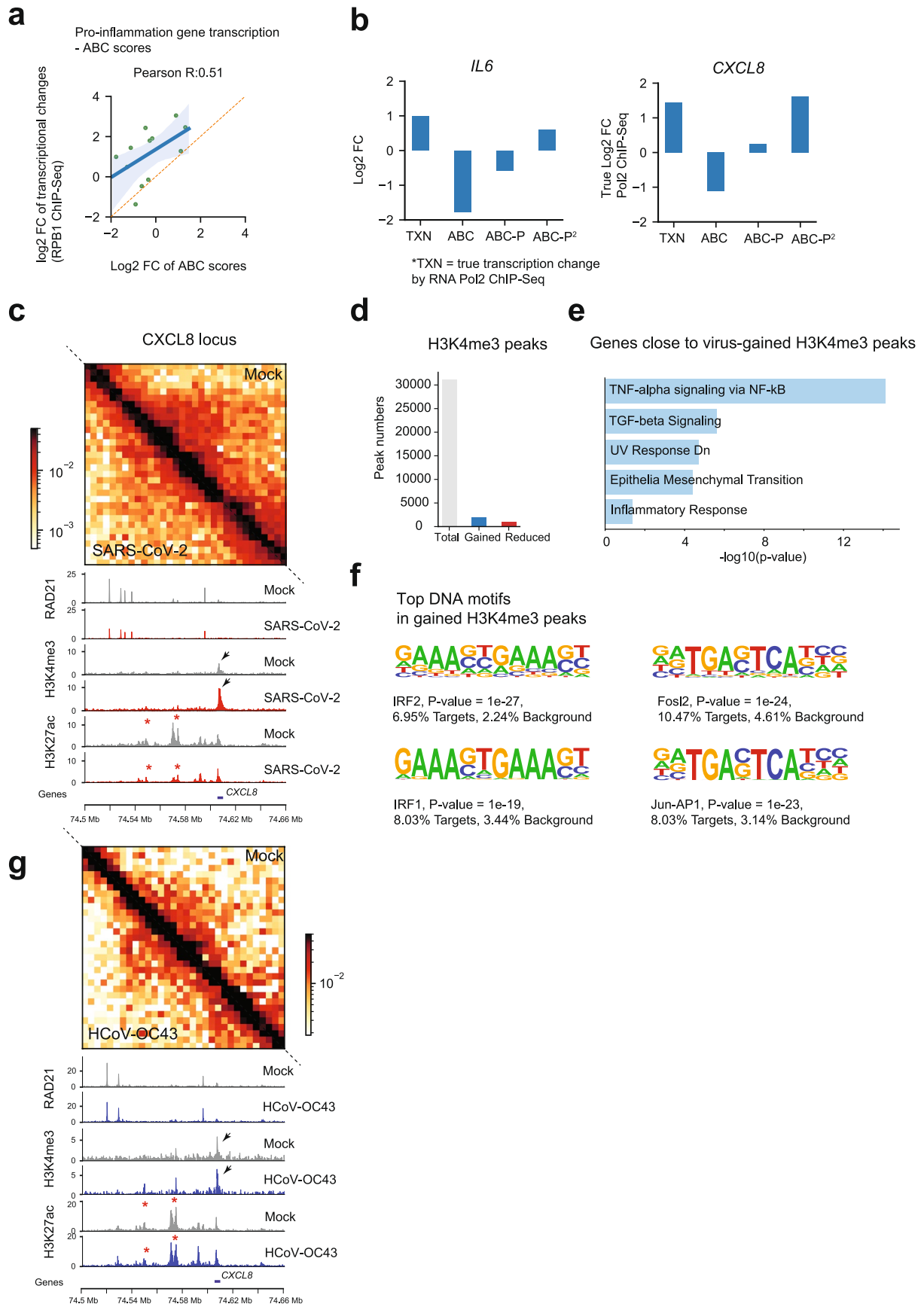
Extended Data Fig. 10 | See next page for caption.

Extended Data Fig. 10 | Pro-inflammatory genes are induced by SARS-CoV-2 infection concurrent with increased promoter activity and H3K4me3 levels.
a. A scatter plot showing good correlation between the ABC score (x-axis) and the true transcriptional changes of pro-inflammatory (PIF) genes by SARS-CoV-2 (y-axis, RPB1 ChIP-Seq). But the quantity of true changes (y axis) is much higher than the modelled changes based on ABC scores (x-axis), as all the data points are above the diagonal (also see Fig. 6c for revised ABC-P^2 scores). Error bands indicate the 95% confidence interval of the regression estimate.
b. Bar graphs showing the fold changes of two key PIF genes, *IL6* and *CXCL8*, in several conditions: true RPB1 ChIP-Seq fold changes after SARS-CoV-2 infection (TXN); fold changes modelled by ABC score; modelled by ABC algorithm with inclusion of promoter H3K4me3 strength (ABC-P); modelled by ABC algorithm with inclusion of a square of promoter H3K4me3 strength (ABC-P^2). Promoter strength is required to revise the ABC algorithm to better model transcriptional increases of PIF genes caused by SARS-CoV-2 infection. **c**. Snapshots of Hi-C matrices (bin size: 5 kb) and calibrated ChIP-Seq tracks for indicated factors at another key gene loci coding for pathologically critical PIF cytokines in COVID-19 patients: *CXCL8* (encoding cytokine IL-8). Red asterisks show reduced H3K27ac peaks. Black arrows show increased H3K4me3 peaks at its promoter by SARS-

CoV-2 infection. The intra-TAD interactions were weakened throughout the TAD. Color scales indicate Hi-C contact frequencies. **d**. Barplot showing the numbers of total, gained or reduced H3K4me3 ChIP-Seq peaks after SARS-CoV-2 infection for 24hpi (0.1 MOI). **e**. Hallmark signature analysis of genes close to H3K4me3 peaks gained in virus-infected condition show signatures associated with TNF-alpha, TGF-beta signaling or inflammatory responses, which are associated with pathological symptoms in COVID-19 patients. **f**. Motif analysis of H3K4me3 peaks increased in SARS-CoV-2 infected cells shows that the top ranked motifs are those of IRF1/2 and Jun/AP1, suggesting the potential roles of these transcription factors in transcriptional activation of inflammation genes. Motif analysis was done by HOMER, and the P values and percentages of sites with motifs are shown. **g**. Snapshots of Mock and HCoV-OC43 Hi-C contact matrices (bin size: 5 kb) and ChIP-Seq tracks for indicated factors at the *CXCL8* (encoding IL-8) loci. This is from the same region as in panel c. In comparison to SARS-CoV-2 effect in panel c, HCoV-OC43 caused no reduction of H3K27ac peaks (Red asterisks), and no obvious H3K4me3 increase at its promoter (black arrows). These asterisks and arrows point to the same peaks as those in panel c. Color scales indicate Hi-C contact frequencies.

nature portfolio

Corresponding author(s): WENBO LI

Last updated by author(s): Jan 31, 2023

Reporting Summary

Nature Portfolio wishes to improve the reproducibility of the work that we publish. This form provides structure for consistency and transparency in reporting. For further information on Nature Portfolio policies, see our Editorial Policies and the Editorial Policy Checklist.

Statistics

For all statistical analyses, confirm that the following items are present in the figure legend, table legend, main text, or Methods section.

n/a	Confirmed	
☐	☒	The exact sample size (*n*) for each experimental group/condition, given as a discrete number and unit of measurement
☐	☒	A statement on whether measurements were taken from distinct samples or whether the same sample was measured repeatedly
☐	☒	The statistical test(s) used AND whether they are one- or two-sided *Only common tests should be described solely by name; describe more complex techniques in the Methods section.*
☒	☐	A description of all covariates tested
☒	☐	A description of any assumptions or corrections, such as tests of normality and adjustment for multiple comparisons
☐	☒	A full description of the statistical parameters including central tendency (e.g. means) or other basic estimates (e.g. regression coefficient) AND variation (e.g. standard deviation) or associated estimates of uncertainty (e.g. confidence intervals)
☐	☒	For null hypothesis testing, the test statistic (e.g. *F*, *t*, *r*) with confidence intervals, effect sizes, degrees of freedom and *P* value noted *Give P values as exact values whenever suitable.*
☒	☐	For Bayesian analysis, information on the choice of priors and Markov chain Monte Carlo settings
☒	☐	For hierarchical and complex designs, identification of the appropriate level for tests and full reporting of outcomes
☐	☒	Estimates of effect sizes (e.g. Cohen's *d*, Pearson's *r*), indicating how they were calculated

Our web collection on statistics for biologists contains articles on many of the points above.

Software and code

Policy information about availability of computer code

Data collection: Bcl2fastq v2.2.0

Data analysis:
ChIP-Seq:
STAR v.2.7.0
MACS2 v 2.1.4
deeptools v 3.1.3
HOMER v 4.11
samtools v 1.12

RNA-Seq:
STAR v 2.7.0
HOMER v 4.11
EdgeR v 3.28.1

Hi-C:
HiC-Pro v 2.11.4
cooltools v 0.4.0
cooler v 0.8.2
higlass v 0.8.0
coolpuppy v 0.9.2

For manuscripts utilizing custom algorithms or software that are central to the research but not yet described in published literature, software must be made available to editors and reviewers. We strongly encourage code deposition in a community repository (e.g. GitHub). See the Nature Portfolio guidelines for submitting code & software for further information.

Data

All manuscripts must include a [data availability statement](#). This statement should provide the following information, where applicable:

- Accession codes, unique identifiers, or web links for publicly available datasets
- A description of any restrictions on data availability
- For clinical datasets or third party data, please ensure that the statement adheres to our [policy](#)

Data generated in this study have been deposited to NCBI GEO (GSE179184, https://www.ncbi.nlm.nih.gov/geo/query/acc.cgi?acc=GSE179184). Raw data from fluorescence microscopy imaging are available at Mendeley (http://dx.doi.org/10.17632/czzb4jb8ss.1). Gene sets are available from GSEA molecular signature database (https://www.gsea-msigdb.org/gsea/msigdb). Source data are provided with this paper.

Field-specific reporting

Please select the one below that is the best fit for your research. If you are not sure, read the appropriate sections before making your selection.

☒ Life sciences ☐ Behavioural & social sciences ☐ Ecological, evolutionary & environmental sciences

For a reference copy of the document with all sections, see [nature.com/documents/nr-reporting-summary-flat.pdf](#)

Life sciences study design

All studies must disclose on these points even when the disclosure is negative.

Sample size	No statistical methods were performed to pre-determine the sample sizes. Samples sizes were based on similar studies in the field. Immuno-blotting were conducted for at least two biological replicates. Hi-C 3.0, ChIP-Seq, and RNA-Seq were conducted with at least two biological replicates.
Data exclusions	No data was excluded.
Replication	All experiments were reproduced reliably in independent setting for at least two or three times.
Randomization	Randomization was not applicable to this study. This is not large-scale sample or clinical study, and experiments were performed on human cell lines with certain conditions/treatment.
Blinding	Blinding was not applicable to this study. Results and analyses are directly linked with the treatment labeling, the aim of which was to assess the molecular differences between conditions/treatment.

Reporting for specific materials, systems and methods

We require information from authors about some types of materials, experimental systems and methods used in many studies. Here, indicate whether each material, system or method listed is relevant to your study. If you are not sure if a list item applies to your research, read the appropriate section before selecting a response.

Materials & experimental systems

n/a	Involved in the study
☐	☒ Antibodies
☐	☒ Eukaryotic cell lines
☒	☐ Palaeontology and archaeology
☒	☐ Animals and other organisms
☒	☐ Human research participants
☒	☐ Clinical data
☒	☐ Dual use research of concern

Methods

n/a	Involved in the study
☐	☒ ChIP-seq
☒	☐ Flow cytometry
☒	☐ MRI-based neuroimaging

Antibodies

Antibodies used	Antibodies for western blotting: GAPDH (Proteintech, 60004-1, 1:2000 dilution), alpha-Tubulin (Sigma, T5168, 1:1000 dilution), RAD21 (Abcam, Ab992, Lot: GR214359-10, 1:1000 dilution), CTCF (Millipore, 07-729, 1:1000 dilution), SMC3 (Abcam, Ab9263, Lot:GR466-7, 1:1000 dilution), Total Histone H3 (Abcam, Ab1791, Lot:GR206754-1, 1:2000 dilution), H3K4me3 (Abcam, Ab8580, Lot: GR3264490-1, 1:2000 dilution), H3K9me3 (Abcam, Ab8898, Lot: GR164977-4, 1:2000 dilution), H3K27ac (Abcam, Ab4729, Lot: GR3357415-1, 1:2000 dilution), and H3K27me3 (Cell Signaling Technology, #9733S, Lot19, 1:2000 dilution); Antibodies for immunofluorescence: SARS-CoV-2 Spike glycoprotein (Abcam, Cat#ab272504, 1:500 dilution) or HCoV-OC43 (EMD Millipore, Cat# MAB9012, 1:200 dilution);

The antibodies used for ChIP-Seq include RNA Polymerase II (RPB1 N terminus, Cell Signaling Technology, #14958S, Lot4, 3uL), RAD21 (Abcam, Ab992, Lot: GR214359-10, 3ug), SMC3 (Abcam, Ab9263, Lot:GR466-7, 3ug), CTCF (Millipore, 07-729, 10ul), H3K4me3 (Abcam, Ab8580, Lot: GR3264490-1, 3ug), H3K9me3 (Abcam, Ab8898, Lot: GR164977-4, 3ug), H3K27ac (Abcam, Ab4729, Lot: GR3357415-1, 3ug), H3K27me3 (Cell Signaling Technology, #9733S, Lot19, 3uL).

Validation

These antibodies were used and validated by multiple previous publications, and have also been validated by their respective vendors.
Validation for each antibodies:
GAPDH: https://www.ptglab.com/products/GAPDH-Antibody-60004-1-Ig.htm
alpha-Tubulin: https://www.sigmaaldrich.com/US/en/product/sigma/t5168
RAD21: https://www.abcam.com/rad21-antibody-ab992.html
CTCF: https://www.emdmillipore.com/US/en/product/Anti-CTCF-Antibody,MM_NF-07-729
SMC3: https://www.abcam.com/smc3-antibody-ab9263.html
Total Histone H3: https://www.abcam.com/histone-h3-antibody-nuclear-marker-and-chip-grade-ab1791.html
H3K4me3: https://www.abcam.com/histone-h3-tri-methyl-k4-antibody-chip-grade-ab8580.html
H3K9me3: https://www.abcam.com/histone-h3-tri-methyl-k9-antibody-chip-grade-ab8898.html
H3K27ac: https://www.abcam.com/histone-h3-acetyl-k27-antibody-chip-grade-ab4729.html
H3K27me3: https://www.cellsignal.com/products/primary-antibodies/tri-methyl-histone-h3-lys27-c36b11-rabbit-mab/9733
Spike glycoprotein: https://www.abcam.com/sars-cov-2-spike-glycoprotein-antibody-coronavirus-ab272504.html
HCoV-OC43: https://www.emdmillipore.com/US/en/product/Anti-Coronavirus-Antibody-OC-43-strain-clone-541-8F,MM_NF-MAB9012
RPB1: https://www.cellsignal.com/products/primary-antibodies/rpb1-ntd-d8l4y-rabbit-mab/14958

Eukaryotic cell lines

Policy information about cell lines

Cell line source(s)

Human lung adenocarcinoma cells A549 expressing human ACE2 (A549-ACE2, #NR53821) was acquired from BEI Resources (Manassas, VA). RAD21-mAID2-mClover HCT116 cells are a gift from Masato Kanemakei lab (National Institute of Genetics, Japan). 293T cells are a gift from Jason Liu lab (UTHealth San Antonio, TX).

Authentication

Cell authentication was not performed after obtaining the cells.

Mycoplasma contamination

Mycoplasma was tested every 6-12 months. No Mycoplasma were detected at any point in any cell line used in this study.

Commonly misidentified lines
(See ICLAC register)

No commonly misidentified cell lines were used in this study.

ChIP-seq

Data deposition

☒ Confirm that both raw and final processed data have been deposited in a public database such as GEO.

☒ Confirm that you have deposited or provided access to graph files (e.g. BED files) for the called peaks.

Data access links
May remain private before publication.

Data generated in this study have been deposited to NCBI GEO (GSE179184, https://www.ncbi.nlm.nih.gov/geo/query/acc.cgi?acc=GSE179184).

Files in database submission

A549-ACE2-CTCF-spiChIP-Seq-24hpi-rep1.bw
A549-ACE2-CTCF-spiChIP-Seq-Mock-rep1.bw
A549-ACE2-H3K27ac-spiChIP-Seq-24hpi-rep1.bw
A549-ACE2-H3K27ac-spiChIP-Seq-24hpi-rep2.bw
A549-ACE2-H3K27ac-spiChIP-Seq-Mock-rep1.bw
A549-ACE2-H3K27ac-spiChIP-Seq-Mock-rep2.bw
A549-ACE2-H3K27me3-spiChIP-Seq-24hpi-rep2.bw
A549-ACE2-H3K27me3-spiChIP-Seq-Mock-rep1.bw
A549-ACE2-H3K27me3-spiChIP-Seq-Mock-rep2.bw
A549-ACE2-H3K4me3-ChIP-Seq-24hpi-rep2.bw
A549-ACE2-H3K4me3-ChIP-Seq-Mock-rep2.bw
A549-ACE2-H3K4me3-spiChIP-Seq-24hpi-rep1.bw
A549-ACE2-H3K4me3-spiChIP-Seq-Mock-rep1.bw
A549-ACE2-H3K9me3-ChIP-Seq-24hpi-rep2.bw
A549-ACE2-H3K9me3-ChIP-Seq-Mock-rep2.bw
A549-ACE2-H3K9me3-spiChIP-Seq-24hpi-rep1.bw
A549-ACE2-H3K9me3-spiChIP-Seq-Mock-rep1.bw
A549-ACE2-RAD21-spiChIP-Seq-24hpi-rep1.bw
A549-ACE2-RAD21-spiChIP-Seq-24hpi-rep2.bw
A549-ACE2-RAD21-spiChIP-Seq-Mock-rep1.bw
A549-ACE2-RAD21-spiChIP-Seq-Mock-rep2.bw
A549-ACE2-RPB1-ChIP-Seq-24hpi-rep3.bw

A549-ACE2-RPB1-ChIP-Seq-IFNb.bw
A549-ACE2-RPB1-ChIP-Seq-Mock-rep3.bw
A549-ACE2-RPB1-ChIP-Seq-Veh.bw
A549-ACE2-RPB1-spiChIP-Seq-24hpi-rep1.bw
A549-ACE2-RPB1-spiChIP-Seq-24hpi-rep2.bw
A549-ACE2-RPB1-spiChIP-Seq-Mock-rep1.bw
A549-ACE2-RPB1-spiChIP-Seq-Mock-rep2.bw
A549-ACE2-SMC3-spiChIP-Seq-24hpi-rep1.bw
A549-ACE2-SMC3-spiChIP-Seq-Mock-rep1.bw
A549-ACE2-CTCF-ChIP-Seq.merged.peak.bed
A549-ACE2-H3K27ac-ChIP-Seq.merged.peak.bed
A549-ACE2-H3K4me3-ChIP-Seq.merged.peak.bed
A549-ACE2-RAD21-ChIP-Seq.merged.peak.bed
A549-ACE2-SMC3-ChIP-Seq.merged.peak.bed
A549-ACE2-NS82-Mock-NIPBL-ChIP-rep2.bw
A549-ACE2-NS82-SARS-CoV2-NIPBL-ChIP-rep2.bw
A549-ACE2-NS93-Mock-NIPBL-ChIP-rep1.bw
A549-ACE2-NS93-SARS-CoV-2-NIPBL-ChIP-rep1.bw
A549-ACE2-NS96-Mock-H3K4me3-spiChIP-rep2.bw
A549-ACE2-NS96-Mock-H3K9me3-spiChIP-rep2.bw
A549-ACE2-NS96-SARS-CoV2-H3K4me3-spiChIP-rep2.bw
A549-ACE2-NS96-SARS-CoV2-H3K9me3-spiChIP-rep2.bw

Genome browser session
(e.g. UCSC)

https://genome.ucsc.edu/s/ahwry/SARS%2DCoV%2D2%2DChIP

Methodology

Replicates

All ChIP-Seq experiments were reproduced reliably in independent setting for at least two or three times.

Sequencing depth

Sample Human uniquely aligned reads Sequencing Length Sequencing Strategy
A549-ACE2 RPB1 Mock rep1 spiChIP-Seq   15,323,174 40 Paired-end
A549-ACE2 RPB1 SARS-CoV-2 rep1 spiChIP-Seq   14,784,357 40 Paired-end
A549-ACE2 CTCF Mock rep1 spiChIP-Seq   10,975,165 40 Paired-end
A549-ACE2 CTCF SARS-CoV-2 rep1 spiChIP-Seq   14,563,492 40 Paired-end
A549-ACE2 RAD21 Mock rep1 spiChIP-Seq   15,025,986 40 Paired-end
A549-ACE2 RAD21 SARS-CoV-2 rep1 spiChIP-Seq   15,677,778 40 Paired-end
A549-ACE2 SMC3 Mock rep1 spiChIP-Seq   15,730,317 40 Paired-end
A549-ACE2 SMC3 SARS-CoV-2 rep1 spiChIP-Seq   15,640,801 40 Paired-end
A549-ACE2 H3K27ac Mock rep1 spiChIP-Seq   12,861,996 40 Paired-end
A549-ACE2 H3K27ac SARS-CoV-2 rep1 spiChIP-Seq   13,823,192 40 Paired-end
A549-ACE2 H3K4me3 Mock rep1 spiChIP-Seq   11,669,479 40 Paired-end
A549-ACE2 H3K4me3 SARS-CoV-2 rep1 spiChIP-Seq   14,991,496 40 Paired-end
A549-ACE2 H3K27me3 Mock rep1 spiChIP-Seq   18,632,794 40 Paired-end
A549-ACE2 H3K27me3 SARS-CoV-2 rep1 spiChIP-Seq   24,244,257 40 Paired-end
A549-ACE2 H3K27ac Mock rep2 spiChIP-Seq   19,971,965 40 Paired-end
A549-ACE2 H3K27ac SARS-CoV-2 rep2 spiChIP-Seq   16,413,350 40 Paired-end
A549-ACE2 H3K9me3 Mock rep1 spiChIP-Seq   23,084,491 40 Paired-end
A549-ACE2 H3K9me3 SARS-CoV-2 rep1 spiChIP-Seq   17,857,204 40 Paired-end
A549-ACE2 H3K27me3 Mock rep2 spiChIP-Seq   16,566,768 40 Paired-end
A549-ACE2 H3K27me3 SARS-CoV-2 rep2 spiChIP-Seq   17,307,104 40 Paired-end
A549-ACE2 RAD21 Mock rep2 spiChIP-Seq   13,165,416 40 Paired-end
A549-ACE2 RAD21 SARS-CoV-2 rep2 spiChIP-Seq   13,913,486 40 Paired-end
A549-ACE2 RPB1 Mock rep2 spiChIP-Seq   11,531,097 40 Paired-end
A549-ACE2 RPB1 SARS-CoV-2 rep2 spiChIP-Seq   8,428,345 40 Paired-end
A549-ACE2 RPB1 Mock rep3 ChIP-Seq   23,128,873 40 Paired-end
A549-ACE2 RPB1 SARS-CoV-2 rep3 ChIP-Seq   24,311,384 40 Paired-end
A549-ACE2 H3K4me3 Mock rep2 ChIP-Seq   13,406,860 40 Paired-end
A549-ACE2 H3K4me3 SARS-CoV-2 rep2 ChIP-Seq   11,792,901 40 Paired-end
A549-ACE2 H3K9me3 Mock rep2 ChIP-Seq   13,572,402 40 Paired-end
A549-ACE2 H3K9me3 SARS-CoV-2 rep2 ChIP-Seq   19,354,681 40 Paired-end
A549-ACE2 CTCF Mock rep2 ChIP-Seq   17,147,267 40 Paired-end
A549-ACE2 CTCF SARS-CoV-2 rep2 ChIP-Seq   16,705,311 40 Paired-end
A549-ACE2 RPB1 Veh ChIP-Seq 21,924,661 40 Paired-end
A549-ACE2 RPB1 IFN-beta 6h ChIP-Seq 36,954,934 40 Paired-end
A549-ACE2 H3K4me3 Mock rep2 spiChIP-Seq 4,469,739 Paired-end
A549-ACE2 H3K4me3 SARS-CoV-2 rep2 spiChIP-Seq 5,405,407 Paired-end
A549-ACE2 H3K9me3 Mock rep2 spiChIP-Seq 5,218,635 Paired-end
A549-ACE2 H3K9me3 SARS-CoV-2 rep2 spiChIP-Seq 3,831,010 Paired-end
A549-ACE2 NIPBL Mock rep1 ChIP-Seq 12,835,097 Paired-end
A549-ACE2 NIPBL SARS-CoV-2 rep1 ChIP-Seq 12,948,057 Paired-end
A549-ACE2 NIPBL Mock rep2 ChIP-Seq 5,075,716 Paired-end
A549-ACE2 NIPBL SARS-CoV-2 rep2 ChIP-Seq 5,029,020 Paired-end

Antibodies

The antibodies used for ChIP-Seq include RNA Polymerase II (RPB1 N terminus, Cell Signaling Technology, #14958S, Lot4), RAD21

Antibodies	(Abcam, Ab992, Lot: GR214359-10), SMC3 (Abcam, Ab9263, Lot:GR466-7), CTCF (Millipore, 07-729), H3K4me3 (Abcam, Ab8580, Lot: GR3264490-1), H3K9me3 (Abcam, Ab8898, Lot: GR164977-4), H3K27ac (Abcam, Ab4729, Lot: GR3357415-1), H3K27me3 (Cell Signaling Technology, #9733S, Lot19),NIPBL (Bethyl, A301-779A, lot#4).
Peak calling parameters	For RAD21,SMC3,H3K27ac, CTCF: MACS2 narrowPeak -q 0.01 For H3K4me3: MACS2 broadPeak -q 0.01
Data quality	ChIP-Seq peaks are called at FDR 1%, merged peak numbers are shown below: CTCF: 45530 peaks H3K27ac: 57033 H3K4me3: 29502 RAD21: 67140 SMC3: 65379
Software	ChIP-Seq: STAR v.2.7.0 MACS2 v 2.1.4 deeptools v 3.1.3 HOMER v 4.11